Agricultural Water Management 267 (2022) 107602

Contents lists available at ScienceDirect

Agricultural Water Management

journal homepage: www.elsevier.com/locate/agwat

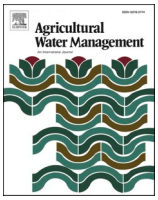

A novel evapotranspiration based irrigation quantification method using the hydrological similar pixels algorithm

Joost Brombacher [a,*], Isadora Rezende de Oliveira Silva [b,c], Jelle Degen [a], Henk Pelgrum [a]

[a] eLEAF B.V., Hesselink van Suchtelenweg 6, 6703CT Wageningen, The Netherlands
[b] G-EAU, Univ Montpellier, AgroParisTech, BRGM, CIRAD, IRD, INRAE, Institut Agro, Montpellier, France
[c] Centre National d'Etudes Spatiales (CNES), Toulouse, France

ARTICLE INFO

Keywords:
Irrigation
Evapotranspiration
Water use
Remote sensing
Hydrological Similar Pixels
ETLook

ABSTRACT

Globally, the agricultural sector is the largest consumer of fresh water, despite the increased efficiency in irrigation. Remote sensing is a valuable tool to monitor agricultural water use. In this study, we demonstrate a novel algorithm that computes high-resolution (10 m) remote sensing-based evapotranspiration (*ET*) data linked exclusively to irrigation, i.e. the incremental evapotranspiration (ET_{incr}). The methodology compares the *ET* of irrigated agricultural pixels to the weighted average *ET* of a subset of natural Hydrological Similar Pixels (HSP). The hydrological similarity is based upon a set of features derived from DEM, soil texture, reference evapotranspiration, and precipitation datasets. The difference in *ET* between the subset of hydrological similar natural pixels and the corresponding irrigated agricultural pixel is explanatory for the amount of *ET* related to irrigation (ET_{incr}). These results are then converted to the water use (m^3) per agricultural field. The method is validated for three study areas in South Africa, Spain, and Australia. Comparing the monthly and seasonal water use estimates to water meter observations in the Hex Valley (South Africa), yielded an R^2 of 0.751 and 0.780, respectively. For the Ebro (Spain) and Namoi (Australia) study areas, the accuracy of the monthly estimates decreased. In Australia, this was a result of the water meters being linked to local reservoirs, instead of the direct use of the irrigation systems. In total, 8 out of the 27 validation fields with monthly data showed a Kling-Gupta Efficiency (KGE) larger than 0.5, which highlights that the temporal variability can be captured well by the model. Generally, seasonal estimates showed to be most accurate, which makes the product suitable for comparison with seasonal water allocations and could help to monitor overconsumption in water-scarce environments.

1. Introduction

Water is a scarce resource and its limited availability is recognized as one of the major threats in the coming decades (World Economic Forum, 2021). Due to climate change, agricultural droughts have increased significantly over the last decades (IPCC, 2021). With agriculture being by far the largest consumer of fresh water, the presence and reinforcement of regulations that prevent individual farmers from overconsuming in water-scarce environments should be a priority for any water management agency (FAO, 2011). However, there is limited control on ground and surface water abstractions worldwide (Foster et al., 2020), and most of the irrigation practices are far from efficient (Jägermeyr et al., 2015). Although advances have been made to improve irrigation efficiency (Koech and Langat, 2018), some argue that this does not necessarily reduce the consumptive water use in the agricultural sector (Linstead, 2018; Perry, 2017). Having a tool that remotely monitors the water use of irrigated cropland could help enforce local regulations, increase (environmental) water availability, gain insight on agricultural water use, and prevent conflicts over resources.

The potential of using satellite data for the agricultural sector is widely acknowledged (Sishodia et al., 2020). Although estimating the water use of irrigated cropland based on satellite data is challenging, multiple studies have been conducted on this topic. Some are primarily based on soil moisture (Brocca et al., 2018; Dari et al., 2020; Jalilvand et al., 2019; Zappa et al., 2021; Zaussinger et al., 2019), and others focus on evapotranspiration estimates (Bretreger et al., 2020; Koch et al., 2020; Romaguera et al., 2012; Tazekrit et al., 2018; Van Eekelen et al., 2015). For these two approaches, different satellite observations are needed. Surface soil moisture is best monitored with low resolution (10–50 km) microwave sensors, such as SMAP, SMOS, and ASCAT (Peng

* Corresponding author.
E-mail address: joost.brombacher@eleaf.com (J. Brombacher).

https://doi.org/10.1016/j.agwat.2022.107602
Received 27 September 2021; Received in revised form 4 March 2022; Accepted 8 March 2022
Available online 1 April 2022

et al., 2021). However, Zappa et al. (2021) demonstrated that an upscaled (500 m) Sentinel-1 based soil moisture product could be used to estimate irrigation amounts accurately. Remote sensing based evapotranspiration models often combine thermal infrared and/or optical multispectral satellite data with meteorological datasets. Evapotranspiration models which require thermal infrared data often have a lower spatial resolution (1 – 10 km) (Koch et al., 2020; Van Eekelen et al., 2015) than models that base their estimates on crop coefficients (Kc) and the reference evapotranspiration (10 – 30 m) (Bretreger et al., 2020; Tazekrit et al., 2018). The mentioned remote sensing based irrigation quantification studies show the potential of using satellite data for water use monitoring. Nevertheless, for modeling the water use of individual fields, they generally lack spatial resolution (Lesiv et al., 2019). Only the studies of Bretreger et al. (2020) and Tazekrit et al. (2018) used evapotranspiration models of sufficient resolution. However, the accuracy of such crop coefficient and reference evapotranspiration based models is often region-dependent and the product is, therefore, less scalable than most other energy balance models (Blatchford et al., 2020). Also, the estimated Kc-based evapotranspiration mimics the evapotranspiration under well-watered conditions, which rarely occur in semi-arid climates, resulting in an overestimation of the actual evapotranspiration (Jovanovic and Israel, 2012; Thoreson et al., 2009). Therefore, more sophisticated energy balance models would be preferred as input for water use estimated models.

Several remote sensing based energy balance models have been developed in the last decades (Zhang et al., 2016). When estimating the evapotranspiration using energy balance models, acquiring land surface temperature (LST) data is often a limiting factor, with only a few platforms providing LST observations with a moderate temporal (< 16 days) and spatial resolution (0.1–1 km) (Zhu et al., 2018). ETLook, the successor of SEBAL, is one of the models that use the Penman-Monteith equation to estimate the actual evapotranspiration. The model partitions the energy available for evaporation (E) and transpiration (T) based on the leaf area index (LAI) and is easily scalable from field to continental extents. In addition, the E and T can be calculated separately in data-scare environments, such as areas with persistent cloud cover. Because the model uses upscaled LST data in combination with high resolution optical satellite data, the resolution of the outputs can be as high as 10 m (Bastiaanssen et al., 2012). This, in combination with the daily temporal resolution, makes the model suitable as an input for generating water use estimates at field level.

ET data alone, however, does not differentiate between irrigated and rainfed *ET*. This partition was the subject of the research of Van Eekelen et al. (2015). In their study, SEBAL (Bastiaanssen et al., 1998) was used to calculate actual evapotranspiration, which was then compared to the ratio between the accumulated evapotranspiration (E) and precipitation (P) for land classes with similar natural conditions. From the E/P ratio, the evapotranspiration originating from precipitation (E_p) was calculated and subtracted from the actual evapotranspiration, to calculate the incremental *ET*. The incremental *ET* was then used to estimate the water use. Although the potential of *ET*-based irrigation quantification was presented, the researchers also experienced some limitations. Acquiring high-resolution precipitation data, for example, is challenging in most regions of the world. In their study, the highest resolution precipitation data had a spatial resolution of 0.1°, which compromised the spatial accuracy of the water use estimates. Another limitation was that the similarity between pixels was purely based on a land-use classification, which generally had an overall accuracy of 85%. Finally, they concluded that ET_p is also impacted by differences in soil type, temporal rainfall distributions, and surface runoff, among others, which were not taken into account at the time.

In this study, we aim to bypass many of the limitations that Van Eekelen et al. (2015) have experienced so we can estimate the water use at field level using remote sensing data. The proposed method uses ETLook to calculate high resolution (10 m) evapotranspiration estimates and the novel Hydrological Similar Pixels (HSP) algorithm to partition between irrigated and natural evapotranspiration. The latter is done by comparing the evapotranspiration of irrigated areas to that of natural pixels that are most similar in hydrogeomorphological conditions and requires satellite-based evapotranspiration data, weather observations, and static environmental datasets. The outcomes are validated for three study areas in South Africa, Spain, and Australia using in-situ water meter observations.

2. Materials and methods

2.1. Water balance

The objective of hydrological dilemmas is often the same: to close the water balance. The water balance is described in Eq. (1), where P represents the precipitation, R the streamflow, ET the evapotranspiration, and ΔS the change in storage, either in the soil, bedrock, or groundwater.

$$P = R + ET + \Delta S \tag{1}$$

In stable systems, ΔS is considered 0, so the equation solely relies on the precipitation, evapotranspiration, and streamflow. However, in many regions, the streamflow is unknown, precipitation data unreliable, and the change in storage is not neglectable, resulting in difficulties when trying to close this equation.

The approach of this research is to use *ET* data to quantify irrigation water use and mimic conditions where all the other terms of the water balance can be neglected. This is done by comparing the *ET* of irrigated crops to the *ET* of non-irrigated natural vegetation. The assumption here is that for areas with similar hydrogeomorphological conditions, the difference in *ET* is solely a result of irrigation efforts (Eq. (2)). This difference in *ET* between natural (ET_{nat}) and irrigated vegetation (ET_{irr}) is called incremental evapotranspiration (ET_{incr}).

$$ET_{incr} = ET_{irr} - ET_{nat} \tag{2}$$

2.2. Irrigation Quantification Method

The proposed irrigation quantification method is divided into three parts, i.e. data collection and (pre)processing, algorithm processing, and irrigation quantification, which are described in Fig. 1. The inputs are either of periodic or static nature. Periodic inputs originate from weather stations and satellites, while static inputs come from digital elevation model (DEM), soil texture, and land cover classification datasets. Based on these inputs, two core algorithms are used. ETLook, developed by Bastiaanssen et al. (2012), is responsible for producing actual (ET_{act}) and reference evapotranspiration (ET_{ref}) data, which together with precipitation data and the static datasets are fed into the Hydrological Similar Pixels (HSP) algorithm. The ETLook model estimates the key hydro-meteorological parameters of the Penman-Monteith equation empirically, based on minimal field and remote sensing data, without the need for numerical simulation methods. This approach leads to adequate quantification of the evapotranspiration (Blatchford et al., 2020). Analogous to the study of Van Eekelen et al. (2015), the base of the HSP algorithm is a high-resolution land cover map that distinguished irrigated agriculture from natural vegetation. The HSP algorithm aims to identify for each irrigated agricultural pixel, a subset of natural pixels that are similar to the irrigated agricultural pixel in terms of precipitation, reference evapotranspiration, topography, and soil texture. The addition of these static and periodic datasets is an improvement upon the approach of Van Eekelen et al. (2015), where only evapotranspiration data, precipitation data, and a land cover map were used to calculate the irrigated water use. The output of the HSP algorithm is the incremental evapotranspiration (ET_{incr}), which describes the amount of water that is evaporated purely due to irrigation. This value is finally converted to the water use (m^3) based on the surface area of a specific field or cluster of fields.

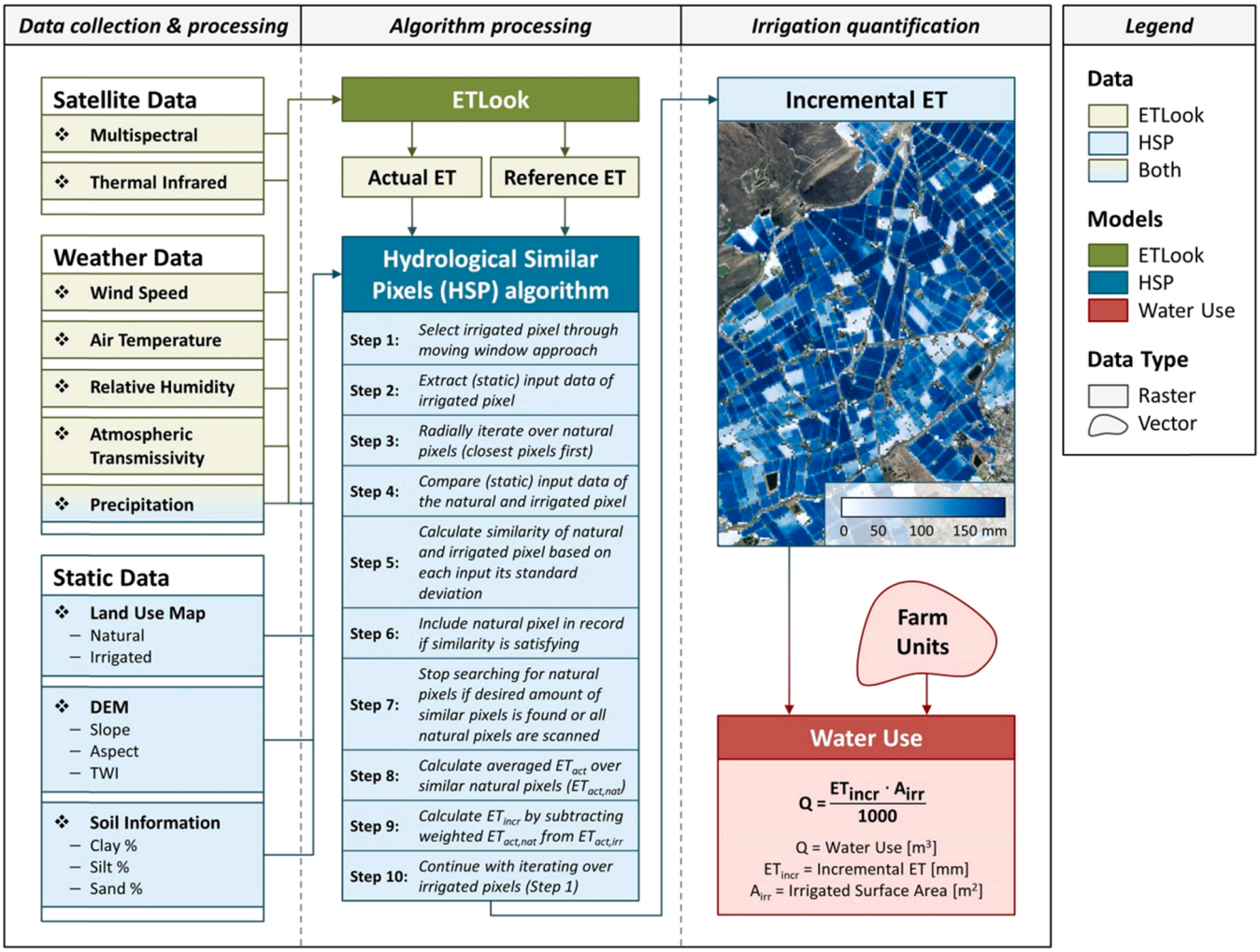

Fig. 1. Flowchart of the irrigation quantification method. As periodic inputs for the ETLook model, thermal and multispectral satellite data and weather observations are used. The HSP method relies, besides periodic precipitation (P), reference evapotranspiration (ET_{ref}), and actual evapotranspiration (ET_{act}) data, also upon static inputs like a high-resolution land cover map to classify natural and irrigated areas, a digital elevation model (DEM) to derive the slope, aspect, and Topographic Wetness Index (TWI), and soil information to derive the percentages clay, silt, and sand in the area. By using ETLook and the HSP algorithm we can derive the incremental evapotranspiration (ET_{incr}), which can be converted to the water use (m^3) per field.

2.2.1. Data collection and processing

The multispectral data used for this research is captured by the Multispectral Imager (MSI) and OLI (Operational Land Imager) sensors, carried by the satellites Sentinel-2A and 2B (ESA, 2012), and Landsat 8 (U.S. Geological Survey, 2015), respectively. The first sensor provides 10 m spatial resolution data every 5 days, while the latter has a 30 m resolution and 16 days overpass frequency. Level 1 C reflectance products were (i) downloaded, (ii) atmospherically corrected (Rahman and Dedieu, 1994), (iii) adjusted according to a surface bidirectional reflectance distribution function (BRDF) (Roy et al., 2006), (iv) topographically normalized (Richter et al., 2009), and (v) cloud masked by an external company, using a deep-learning model and manual accuracy check (www.cloudisnoise.com). The corrected reflectances were employed to calculate the normalized difference vegetation index (NDVI) and the albedo, which are inputs for the ETLook model.

As thermal data, the brightness temperature from Visible Infrared Imager and Radiometer Suite (VIIRS) onboard of SUOMI NPP (Roger et al., 2017) was employed. For this wavelength, the images have a 375 m resolution and are provided daily. To estimate the weekly land surface temperature (LST), the least clouded image per week was used. To better capture the variability within the images, a lookup table between high and low-resolution albedo and NDVI was built and extrapolated to upscale the LST data.

The meteorological information required for the processing comes from the most recent validated Atmospheric General Circulation Model from the Earth model and data assimilation system Goddard Earth Observing System (GEOS) of the National Aeronautics and Space Administration (NASA) (Rienecker et al., 2008). When available, data from local meteorological stations was also collected. That was the case for some meteorological variables in Australia, which were available via the Bureau of Meteorology (www.bom.gov.au), and the weather services of Hortec (www.hortec.co.za), for the Western Cape, South Africa. The transmissivity was computed from the incoming shortwave radiation products distributed by the geostationary satellites MSG (ESA, 1999) and Himawari (Japan Meteorological Agency, 2015). Temperature and humidity variables from GEOS were disaggregated according to Rouf et al. (2020), while station data was spatially interpolated following the work of Hengl (2007).

The static inputs dictate most of the similarity between natural and irrigated pixels. To be able to exploit the algorithm on a global level, only globally available datasets were considered. An overview of them is given in Fig. 2.

The first set of static features used in the HSP algorithm are features derived from a digital elevation model (DEM) since it is acknowledged

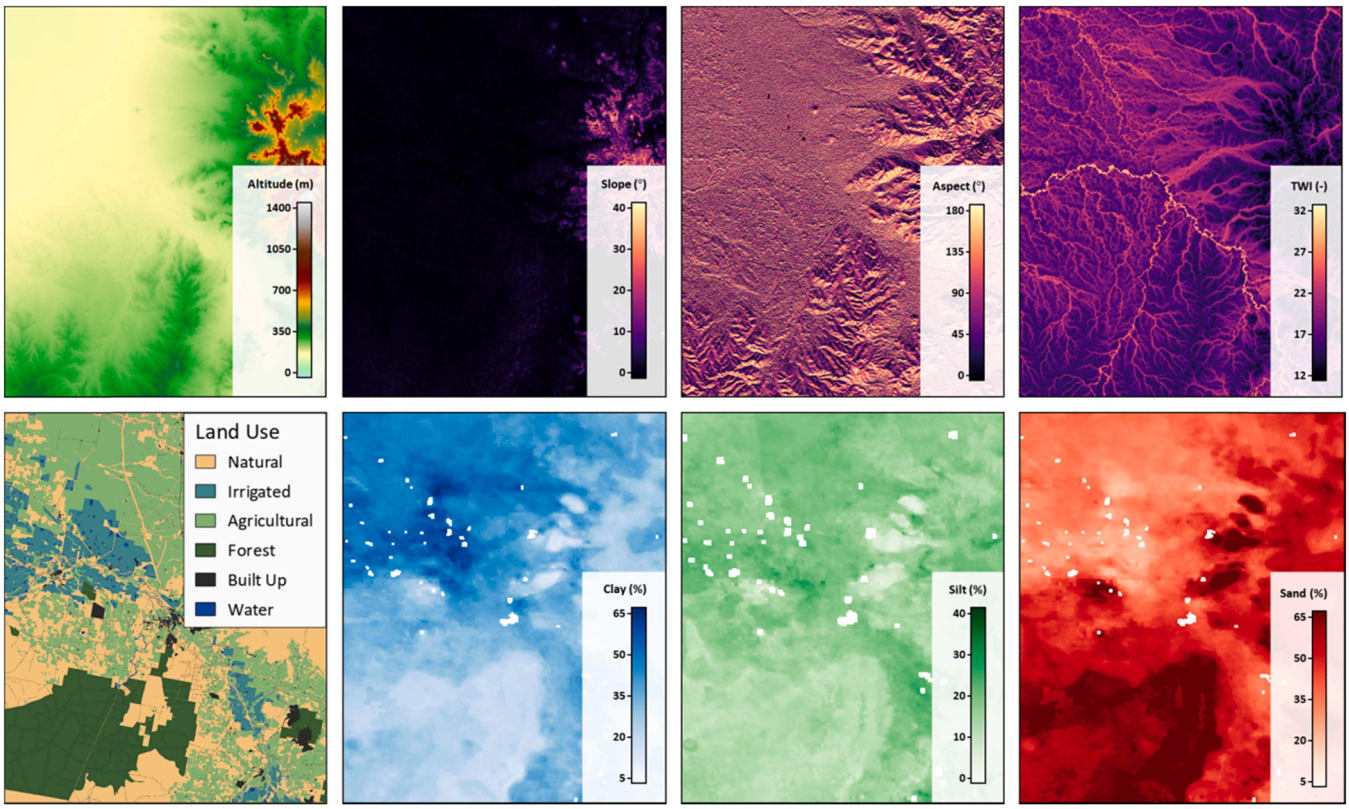

Fig. 2. An overview of the static features used for the Hydrological Similar Pixels (HSP) algorithm, consisting of the slope, aspect, and Topographic Wetness Index (TWI), derived from the Shuttle Radar Topography Mission (SRTM) DEM; clay, silt, and sand percentages derived from the ISRIC SoilGrids database (Hengl et al., 2017); and the land cover classification, whose source depends on the study area. These examples are illustrating the static features of the area surrounding Narrabri, New South Wales, Australia.

that topography, in general, can be an excellent indicator for hydro-geomorphological differences (Noh et al., 2015). The DEM used for this research is provided by the Shuttle Radar Topography Mission (STRM) dataset, which covers 80% of the world's landmass at 30 m resolution (Hennig et al., 2007). The DEM-based static features are the slope, aspect, and Topographic Wetness Index (TWI). The aspect is converted from a 360° to a north-south (180°) orientation since the east and west orientation does not usually explain the difference in available solar radiation. The TWI is often used as an index to account for differences in hydrological processes due to topography (Sørensen et al., 2006), and was first derived by Beven and Kirkby (1979). The TWI is calculated using the SAGA-GIS flow accumulation module (Conrad et al., 2015). The TWI typically ranges between –3 and 30, with low values indicating dry and high values indicating wet conditions.

The second set of static features is related to the soil type. The soil type is chosen due to its effect on the storage of nutrients, infiltration capacity, rooting depth, capillary rise, field capacity, and wilting point, to name a few (Moene and Dam, 2014). The ISRIC SoilGrids database provides global pH, bulk density, coarse fragments content, sand content, silt content, clay content, cation exchange capacity (CEC), total nitrogen, as well as soil organic carbon density, content, and stock, at 250 m resolution (Hengl et al., 2017). For this research, the clay, silt, and sand content were considered.

The choice of the land cover map depends on the study area, but generally, the highest resolution and the most up-to-date public datasets are chosen. The minimum requirements for a land cover map are the spatial resolution (< 30 m) and the presence of the classes: (i) rain-fed and (ii) irrigated agriculture, (iii) built-up areas, (iv) open water bodies, (v) natural and (vi) forest areas. For the HSP algorithm, the forest areas should not be included as comparable natural areas. Trees are generally more resilient to drought and have better access to water than crops. As a result, they tend to show higher evapotranspiration rates than crops during water-stressed conditions, causing underestimated or even negative ET_{incr} values. For South Africa we used the South African National Land-Cover (SANLC) 2018 dataset (Thompson, 2019), for Spain the Sistema de Información sobre Ocupación del Suelo de España (SIOSE) dataset (SIOSE, 2018), and for Australia the New South Wales Landuse 2017 v1.2 dataset (DPIE, 2020).

2.2.2. *Algorithm processing*

The ETLook algorithm requires, besides meteorological data, satellite data on NDVI, surface albedo, and soil moisture. The soil moisture is derived using land surface temperature (LST) and NDVI data according to the methodology described by Yang et al. (2015), which uses a trapezoid approach on a pixel-by-pixel basis. A thorough validation of the ETLook algorithm for multiple use cases (field level, regional level, and continental level) is done by Blatchford et al. (2020).

The HSP model aims to find, for each irrigated agricultural pixel, a subset of hydrological similar natural pixels. This similarity is expressed as the difference per static input between the natural and agricultural pixels compared to its standard deviation over the entire study area (Eq. (3)). For example, in a mountainous area, the standard deviation of the slope is high, so pixels are considered to be similar earlier compared to pixels in a flat area. This choice is made to enable flexibility in the definition of similar pixels, but also to make sure that in every environment similar pixels can be found. The similarity score of every static input is then averaged to compute the general similarity (Eq. (4)).

$$s_{feat} = 1 - \frac{abs(irr_{feat} - nat_{feat})}{\sigma_{feat}} \quad (3)$$

$$s = \frac{s_{slope} + s_{aspect} + s_{TWI} + s_{clay} + s_{silt} + s_{sand}}{N_{feat}} \tag{4}$$

Here, s_{feat} represents the score per static feature, namely slope, aspect, TWI, clay, silt, and sand contents. irr_{feat} is the feature value of the irrigated pixel; nat_{feat} the value of the natural pixel; σ_{feat} the standard deviation calculated for the entire scene; s the overall score of all static inputs.

A natural pixel is considered similar if the score is larger than the threshold (*thr*) parameter, which is expressed as:

$$thr = -thr_{std} + 1 \tag{5}$$

In which thr_{std} expresses the number of standard deviations the score is allowed to deviate from to be considered similar. If this similarity is above a predefined threshold, the natural pixel will be added to the subset of similar pixels (Eq. (6)).

$$similar = \begin{Bmatrix} s \leq thr: & False \\ s > thr: & True \end{Bmatrix} \tag{6}$$

Not all static inputs are prepared in the same manner before calculating the similarity. The aspect is only an important feature when there is a significant slope, as in (relatively) flat regions, the difference in solar radiation caused by the aspect is negligible. Therefore, for irrigated agricultural pixels with a slope smaller than 2°, the aspect is considered not of interest. This is reflected by indicating the allowed aspect error to be 180°, meaning that even if the aspect difference between the natural and irrigated pixels is 180°, the aspect of those pixels is still considered similar. For irrigated agricultural pixels with a slope larger than 2°, an exponential function is used to decrease the allowed aspect error when the slope increases. Both scenarios are described by Eqs. (7) and (8).

$$e_{aspect} = \begin{Bmatrix} irr_{slope} < 2: & 180 \\ irr_{slope} \geq 2: & 180e^{-0.115\left(irr_{slope}-2\right)} \end{Bmatrix} \tag{7}$$

$$s_{aspect} = 1 - \frac{abs(irr_{aspect} - nat_{aspect})}{e_{aspect}} \tag{8}$$

In addition to the scores of each static input, for each natural pixel that passes the similarity criteria, the Total Available Water (*TAW*) is calculated. *TAW* reflects the impact of the soil type on the water holding capacity of the soil, which depends on the field capacity, permanent wilting point, and rooting depth (Mohamed and Ali, 2006). Since the rooting depth is unknown, this parameter has a constant value and is expressed as a ratio of the rooting depth of natural vegetation compared to that of crops. Generally, for irrigated crops, this value is set to 1 and for natural crops this value is set to 1.5, meaning that natural vegetation root 1.5 times deeper than crops, mainly due to natural vegetation being better suited for dry conditions. These values are chosen after calibration of the HSP algorithm using in-situ water meter observations. Effectively, the *TAW* scales the ET_{act} of natural vegetation to be more comparable to the ET_{act} of irrigated agricultural vegetation. For the calculation of the *TAW*, pedotransfer functions derived by Mohamed and Ali (2006) are used, which calculate the field capacity (q_{FC}) and permanent wilting point (q_{PWP}) using sand, silt, and clay fractions. Coupled with the rooting depth (z_{root}), the *TAW* is calculated according to Eq. (9).

$$TAW = 1000(q_{FC} - q_{PWP})z_{root} \tag{9}$$

The *TAW* is calculated for both the irrigated agricultural and the natural pixels that meet the similarity criteria. By dividing the *TAW* of the natural pixel (TAW_{nat}) with the *TAW* of the irrigated agricultural pixel (TAW_{irr}), the TAW_{ratio} is calculated. This ratio is used to scale the ET_{act} of the natural pixels to match the ET_{act} of the irrigated agricultural pixel, as shown in Eqs. (10) and (11).

$$TAW_{ratio} = TAW_{nat}/TAW_{irr} \tag{10}$$

$$ET_{act_{nat,adj}} = ET_{act_{nat}}/TAW_{ratio} \tag{11}$$

As an additional criterion for natural pixels to be considered similar to the irrigated agricultural pixel, the scores of the reference evapotranspiration (ET_{ref}) and precipitation (P) are calculated. These are calculated in the same way as expressed in Eq. (3). The score of the ET_{ref} and P are then combined to a single feature by calculating the mean score of the two. This step is done separately from the static input because pixels might be completely similar in a geomorphological manner, but experience different conditions due to local rainfall events or increased evapotranspiration due to differences in solar radiation. Once the combined score of ET_{ref} and P is above 0, meaning that the difference between the ET_{ref} and P of the natural pixel is smaller than the averaged standard deviation of the two, a natural pixel is finally considered hydrologically similar to its irrigated agricultural counterpart.

For each irrigated agricultural pixel, the algorithm loops over all the natural pixels in a spiral manner, starting close to the irrigated pixel. The "thr_nsimpix_max" parameter tells the algorithm how many similar natural pixels have to be found per irrigated pixel. Once this number is met, or all the natural pixels are handled, the algorithm stops looking for natural pixels and continues to the next irrigated pixel. Because this process is computationally expensive, the raster data is processed per block and the Numba library (Lam et al., 2015) is used to drastically increase the processing speed. To decrease the runtime even further, before running the HSP algorithm, per irrigated agricultural pixel the distance to the closest natural pixels is calculated and stored in a raster. This enables the HSP algorithm to start searching for similar natural pixels at the minimum known distance to a natural pixel for each irrigated agricultural pixel.

Once the HSP algorithm is done looping over all the natural pixels, the stored scores and distances are normalized so they range between 0 and 1. With 1 indicating perfect similarity and 0 indicating the lowest allowed similarity. This normalization is, for the static scores, based on the *thr* parameter and for the distances based on the maximum distance. The non ET_{ref} and P scores are normalized based on the minimum and maximum scores found for those inputs, per study period. Normalizing these scores enables one to generate a total score for each natural pixel, which is used as a weight to calculate a weighted ET_{act} for all the natural pixels. This weighted ET_{act} favors natural pixels with high total scores over natural pixels with lower scores. The weighted natural ET_{act} is then subtracted from the ET_{act} of the irrigated agricultural pixel, which yields the incremental evapotranspiration (ET_{incr}). These steps are explained in Eqs. (12)–(15).

$$s_{per,norm} = \frac{s_{per} - s_{per,min}}{s_{per,max} - s_{per,min}}$$

$$s_{stat,norm} = \frac{s_{stat} - thr}{1 - thr} \tag{12}$$

$$s_{dist,norm} = \frac{s_{dist} - s_{dist,min}}{s_{dist,max} - s_{dist,min}}$$

$$w = \frac{s_{per,norm} + s_{stat,norm} + s_{dist,norm}}{3} \tag{13}$$

$$ET_{act_{nat,weighted}} = \sum_{i=1}^{n_{similar}} \frac{ET_{act_{nat}}(i)w(i)}{\sum w} \tag{14}$$

$$ET_{incr} = ET_{act_{irr}} - ET_{act_{nat,weighted}} \tag{15}$$

Here, s_{per} represents the score of the periodic (ET_{ref} and P) inputs, s_{stat} the score of the static inputs (slope, aspect, TWI, and sand, silt, and clay content), and s_{dist} the score of the distance, which are all expressed as an array based on the subset of most similar natural pixels. The weight (w) is calculated for the normalized s_{per}, s_{stat}, and s_{dist}, and used to calculate

the weighted ET_{act} for all the natural pixels in the subset. The incremental evapotranspiration (ET_{incr}) is then calculated by subtracting $ET_{act_{nat.weighted}}$ from the ET_{act} of the irrigated pixel ($ET_{act\,irr}$). At this point, the algorithm is ready to loop over the next irrigated agricultural pixel.

2.2.3. Irrigation quantification

The ET_{incr} is expressed in mm, similar to the ET_{act}. To convert this unit to volumes, the ET_{incr} is multiplied by the area of the agricultural field. A prerequisite for calculating the water use is that, per operational unit, either being fields, a cluster of fields, or catchments, the perimeter of these operational units is known. However, at field level, those shapes are often not only showing agricultural fields, but instead are linked cadastral units, including roads, houses, reservoirs, and other non-agricultural areas. To increase the accuracy of the water use estimates, the same land cover map that is used to distinguish natural and irrigated agricultural pixels is used to calculate the area of irrigated agriculture (A_{irr}) within each operational unit. This area (m^2) is then used to convert the ET_{incr} (mm) to the water use (Q) in m^3. This process is explained by Eq. (16).

$$Q = \frac{ET_{incr}\, A_{irr}}{1000} \tag{16}$$

2.3. Statistical analysis

To assess the accuracy of the estimated water use, multiple statistical metrics were obtained. To assess the goodness of fit between the observed and estimated water use, the coefficient of determination (R^2) and the root mean squared error (RMSE) were calculated. The RMSE is chosen as an additional metric since it is expressed in the same unit as the modeled outputs and has a strong foundation in model evaluation studies (Chai and Draxler, 2014). The R^2 and RMSE were calculated using the Scikit Learn (sklearn) package (Pedregosa et al., 2011). Additionally, a significance analysis for all the calculated coefficients of determination was performed using the statsmodels package (Seabold and Perktold, 2010). To prove the significance of the calculated R^2-values, the corresponding p-values should be larger than α, which was set to 0.05. Finally, the deviation between the seasonal observations and estimates (D_i) was calculated. This metric, which is expressed in percentages, shows per individual field the accuracy of the product. Except for the deviation, all the statistical metrics were calculated both on a monthly and seasonal timestep.

We also introduce a different metric to show the temporal accuracy of the monthly estimates, i.e. the Kling-Gupta efficiency (KGE). The KGE combines the correlation coefficient (r), the variability error (a), and the bias error (b), which makes it an ideal metric for time series accuracy assessment (Gupta et al., 2009). The KGE ranges from -∞ to 1, with 1 indicating a perfect fit. For the well-established Nash-Sutcliffe efficiency (NSE), a hydrological model is considered to have a reasonable performance when the NSE is higher than 0, with NSE = 0 indicating that the mean of the predictions is similar to the mean of the observations. For the KGE, when using the same criteria, the threshold between a poorly performing and reasonable model lies at a KGE of −0.4 (Knoben et al., 2019).

2.4. Study areas

Currently, the proposed irrigation quantification method is implemented in the operational Water Auditing application and used in South Africa by several Catchment Management Authorities (CMA's) (ESA, 2021). However, this operational product delivers medium resolution (250 m) data and is mostly used for monitoring large-scale systems. The first study area where a high resolution (10 m) version of the product was applied is the Hex Valley, a highly productive region in the Western Cape, South Africa. To test the accuracy of the application outside South Africa, two additional validation sites were chosen, i.e. the Ebro Basin in Catalonia, Spain, and the Namoi River Catchment in New South Wales, Australia (Fig. 3).

2.4.1. Hex Valley, Western Cape, South Africa

The Hex River Valley is located in the Breede River Catchment in the Western Cape Province. The valley is a relatively narrow valley with a length of 25 km and a maximum width of 4 km, bounded by high mountain ranges on either side (Fig. 3).

The area is classified as a cold semi-arid climate (BSk) by the Köppen-Geiger system. In De Doorns, a town located in the center of the valley, the average annual temperature is 17.2 °C. The warmest month is February at 23.9 °C and the coldest month is July at 9.9 °C. The annual precipitation is 240 mm, with February being the driest (~10 mm) and June the wettest (~30 mm) (Muñoz-Sabater, 2019). The agricultural activities in the Hex River Valley are centered around the commercial cultivation of table grapes which are grown on 5,200 ha of land. The source of irrigation is either originating from surface water (40%) or groundwater (60%) (Ncube, 2018).

In total, for 15 fields, seasonal water meter observations were provided by the Hex Valley Water Users Association, covering September 2018 until May 2019. For 12 out of the 15 fields, weekly data was also made available and converted to a monthly interval.

2.4.2. Ebro Basin, Catalonia, Spain

The Ebro River basin is the largest Mediterranean basin of the Iberian Peninsula, the river has the highest natural mean discharge in Spain. The catchment is enclosed by the Cantabrian Range and the Pyrenees on the north, and by the Iberian Mountains on the south. An extensive irrigation network was built to store and transport Pyrenean water to the plains to sustain the irrigated area that covers around 45% of the basin (Milano et al., 2013).

The study area is located in the eastern part of the Ebro catchment surrounding the town Lleida, focusing around the Urgell and Algerri Balaguer Canals, and is roughly 9,000 km^2 in size (Fig. 3). The climate is a humid subtropical climate (Cfa). The mean maximum summer and winter temperatures are 23.0 °C and 3.5 °C, respectively. The average annual precipitation is 680 mm, with the lowest monthly precipitation in February (~30 mm) and the highest in September (~80 mm) (Muñoz-Sabater, 2019).

Dominant crop types in the area are wheat, corn, and alfalfa. Perennial crops are mainly fruit trees, olive trees, and vineyards. Irrigation is applied either using inundation, drip, or sprinkler systems (Gao et al., 2018).

Daily water meter data was made available by the Institute of Agrifood Research and Technology (IRTA) from April until September 2020, for an apple orchard and two vineyards.

2.4.3. Namoi River, New South Wales, Australia

The Namoi catchment is part of the Murray Darling basin and is completely situated in New South Wales, Australia. The catchment is 43,000 km^2 and the average discharge of the river at the outlet is 25 m^3/s (Arshad et al., 2014; Barma Water Resources et al., 2012). The study area of this research, as shown in Fig. 3, is located between the towns of Narrabri in the northwest, and Boggabri in the southeast. Agriculture is mainly practiced next to the river. The area also includes some nature reserves. In the southeast of the study area, the Boggabri Coal mine is situated, it abstracts approximately 270,000 m^3 of groundwater per year (Herron et al., 2018). Farmers are mostly reliant on groundwater, but surface water is also extracted through permits. In times of high discharges, surface water can also be accessed without registration, which is called supplementary water (Arshad et al., 2014; Barma Water Resources et al., 2012). The climate in the area is a humid subtropical climate (Cfa). The mean maximum summer and winter temperatures are 33.8 °C and 18.0 °C, respectively. The average annual precipitation sum is 650 mm, with precipitation amounts peaking in summer (~80 mm/month) and being lowest in winter (~40 mm/month)

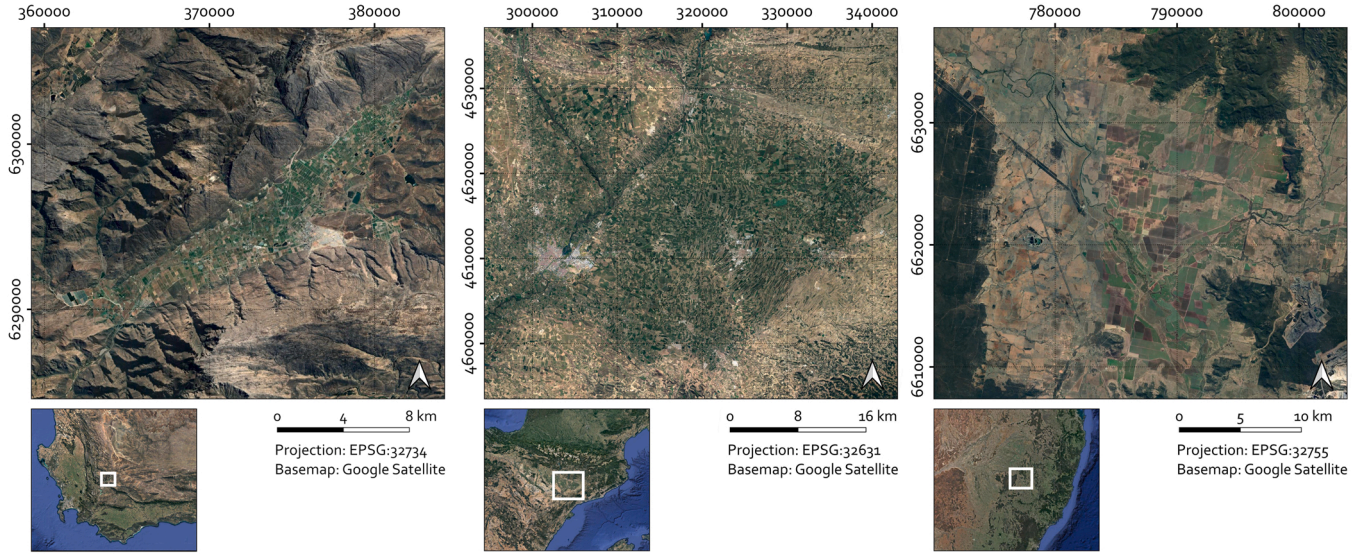

Fig. 3. The Hex Valley study area (left), located in the Western Cape, South Africa; the Ebro basin study area (middle), located in Catalunya, Spain; and the Namoi river study area (right), located in New South Wales, Australia.

(Bureau of Meteorology, 2021). Furrow irrigation is the main type of irrigation in the area, and the furrows are fed with water that is stored in local reservoirs.

The water meter observation data was provided by Water Technology (www.watertech.com.au) and was based on cadastral data (Lots) from the NSW Land Registry Service (LRS) and spreadsheets provided by the Department of Planning and Environment (DPE). The dataset consists of 69 clusters, and each cluster consists of multiple agricultural fields. However, from the 69 available clusters, not all clusters contained areas that were classified as irrigated agriculture, and thus for those clusters no water use estimates were generated. Effectively, 12 of the 69 clusters contained both water meter observations and water use estimations, and these clusters were the focus of the validation study. The study period started in July 2017 and ended in June 2018.

3. Results

To validate the results of the Water Auditing application, we compared our water use estimates to the water meter observations of the three study areas. For all the study areas, both the monthly and the seasonal accumulated water use estimates were included in the comparison. To anonymise the water meter data, the field identifiers are altered to a generic format that starts with the area code (i.e. HEX, EBR, or NAM), followed by a number.

3.1. Hex Valley, Western Cape, South Africa

Fig. 4 shows the accumulated water use estimations for the 2018–2019 season. The ET_{incr} ranged from 200 to 1000 mm. Although

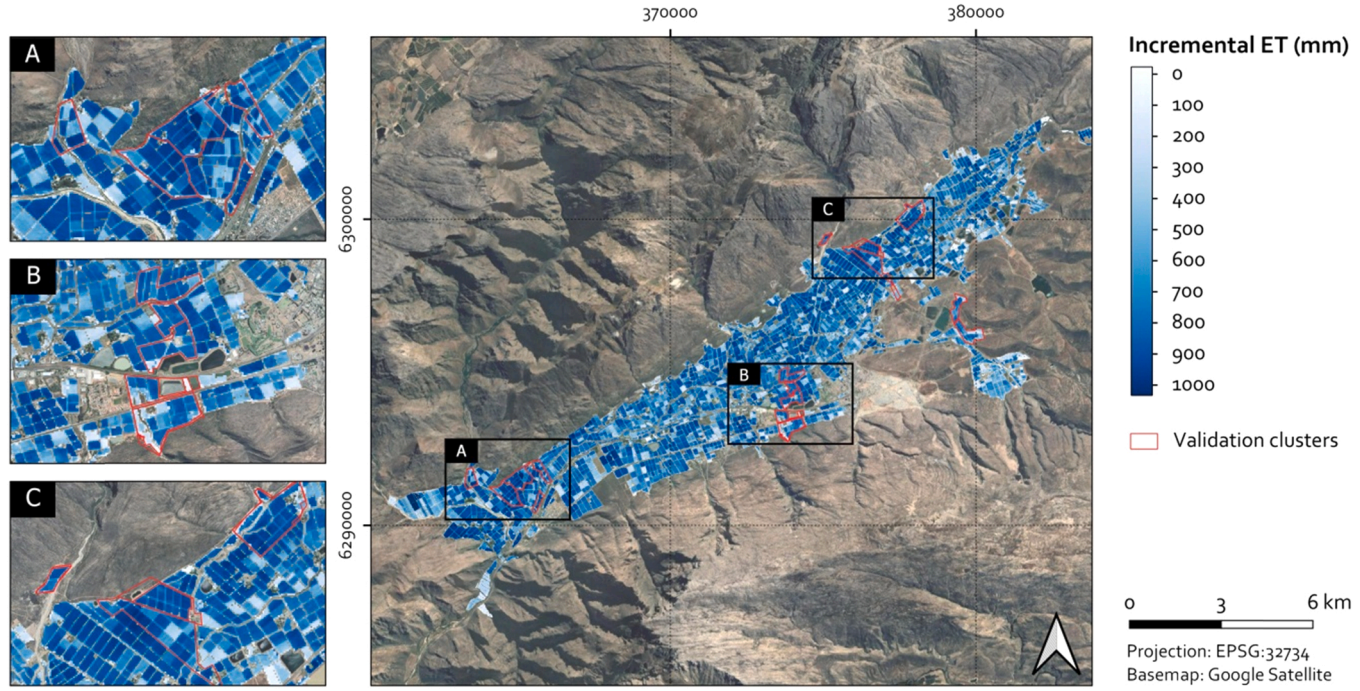

Fig. 4. The accumulated seasonal water use estimates (ET_{incr}) for the Hex Valley during the 2018–2019 season.

the main crop type in the area is table grapes, there were quite some local differences in the estimated water use. Even within each field unit, the estimated water use ranges significantly, indicating the importance of having a high-resolution product when dealing with relatively small fields.

Fig. 5 shows the correlation between the monthly and seasonal water use estimates compared to the observed water use.

For both the monthly and seasonal products, there was a strong correlation between the observed and estimated water use, with an R^2 of 0.751 and 0.780 respectively. Both coefficients of determination showed to be significant ($p \ll 0.05$). Moreover, the trendline was close to the 1:1-line, indicating that there is no general over or underestimation. The correlation for the monthly estimates was lower compared to the seasonal product, which could indicate that the timing of the water use estimates is not always correct. For the seasonal product, 6 of the 15 fields showed a deviation lower than 20%. The error was generally larger for fields with lower observed water use, compared to the one for large consumers.

3.2. Ebro Basin, Catalonia, Spain

For the Ebro region, the seasonal accumulated ET_{incr} estimates ranged between 0 and 800 mm (Fig. 6), while the maximum averaged monthly assessment was about 130 mm/month. The monthly value is analogous to the one of the Hex Valley (~110 mm/month). This illustrates that for equivalent regions in terms of climate comparable evapotranspiration amounts linked to irrigation can be expected.

Despite the size of the study area, only three water meter observations were available for this research. Fig. 7 shows that, for these three plots, the monthly water use estimates were inaccurate. The corresponding R^2 and p-value were 0.051 and 3.68e-05, respectively. Because of the limited amount of validation data, the seasonal results were not statistically significant ($p = 0.084$). The seasonal product showed that the water use of EBR-3 was accurately estimated (0.5% deviation), the water use of EBR-2 was moderately overestimated (23.3% deviation), and the water use of EBR-1 was highly underestimated (53.9% deviation). Both EBR-2 and EBR-3 are vineyards, and their errors are in the same range as the vineyards of the Hex Valley (Fig. 6). EBR-1, on the other hand, is an apple orchard, which might be explanatory for the large deviation. For this study area, the timing issues for the monthly water use estimates were also visible, similar to the results for the Hex Valley.

3.3. Namoi River, New South Wales, Australia

For the Namoi area, the maximum estimated incremental evapotranspiration was 600 mm over the entire season, which translated to an average maximum of 50 mm/month (Fig. 8). This amount is significantly lower compared to the Ebro and Hex Valley regions. This disparity could be linked to the differences in crop types, with perennial crops being abundant in the Ebro and Hex Valley regions, while in Namoi annual crops are dominant. In Fig. 9, similar to the other validation areas, the large spatial variability between fields was also visible.

For these 12 clusters, resembling the findings in the Ebro basin, the monthly estimates did generally not correspond accurately with the water meter observations (Fig. 9). With an R^2 of 0.151, the quality of the estimates was higher compared to the Ebro basin but much lower compared to the Hex Valley. Also, the trend line shows that, generally, the water use is underestimated for this region. Especially for low water use observations, the deviations are large. However, the seasonal product shows that, despite the low monthly accuracy, the accumulated water use corresponds better with the observations (R^2 of 0.406). Both coefficients of determination were statistically significant ($p < 0.05$).

3.4. Study area comparisons

Tables 1, 2, and 3 show the general statistics of the monthly and seasonal water use estimates per field/cluster of the Hex Valley, Ebro, and Namoi study areas, respectively.

Within each table, the last row shows the mean of the estimated and observed water use per study area. For the Hex Valley the mean difference between the estimated and observed water use was 4.5%, indicating that, on a spatiotemporal scale, the model is performing well. For the Ebro and Namoi study areas, this difference was 13.8% and 21.9%, respectively, indicating a lower agreement with regional seasonal water use observations. For both study areas, the water use is generally underestimated. The mean deviation (D_i) for the Hex Valley and Ebro study areas was comparable, with 26.4% and 26.9%, respectively. For the Namoi study area, the mean deviation was larger, with 47.8%. When combining the water use estimates and observations of all the three study areas, the water use was underestimated by 18.8%.

For 2 out of the 30 fields, the KGE is below −0.4. The KGE value for NAM-5 is −0.585, while the one for NAM-12 is −0.560. In total, there are 6 fields with a negative KGE, and 8 with a KGE above 0.5. For the Hex Valley and the Ebro study areas, the mean KGE is 0.385 and 0.405, respectively, indicating that the temporal water use patterns were reasonably well modeled. In contrast, the mean KGE of the Namoi area was only 0.092. Furthermore, 5 of the 6 negative KGE values originate

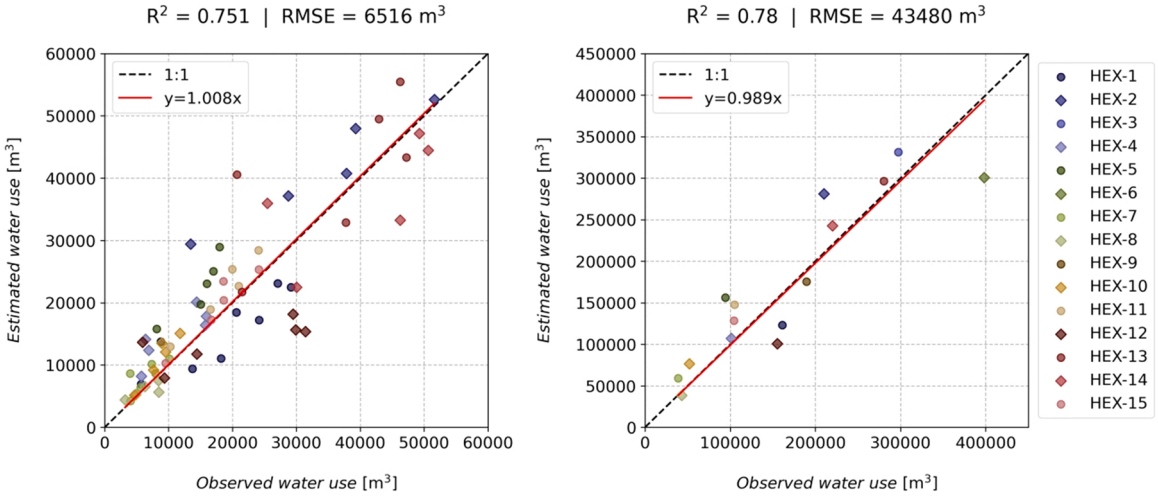

Fig. 5. The estimated water use compared to the observed water use for the Hex Valley at a monthly (left) and seasonal (right) time step.

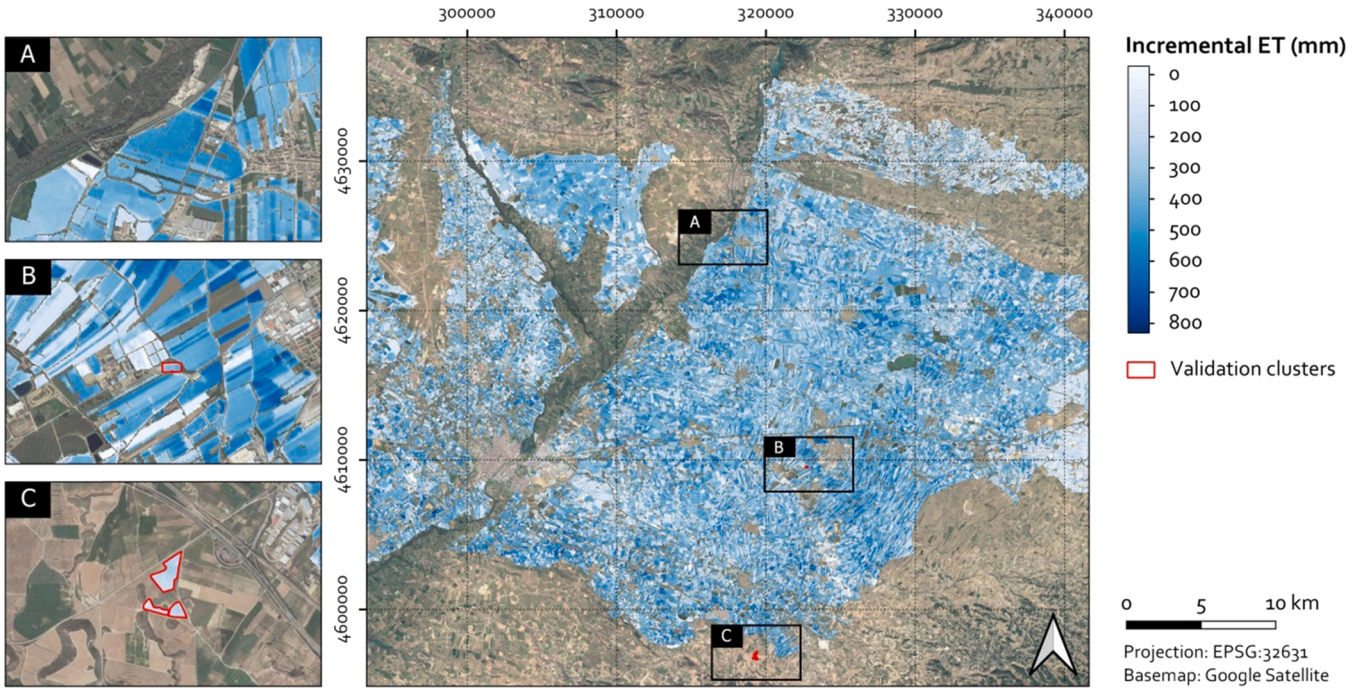

Fig. 6. The accumulated seasonal water use estimates (ET_{incr}) for the Ebro study area during the 2020 season.

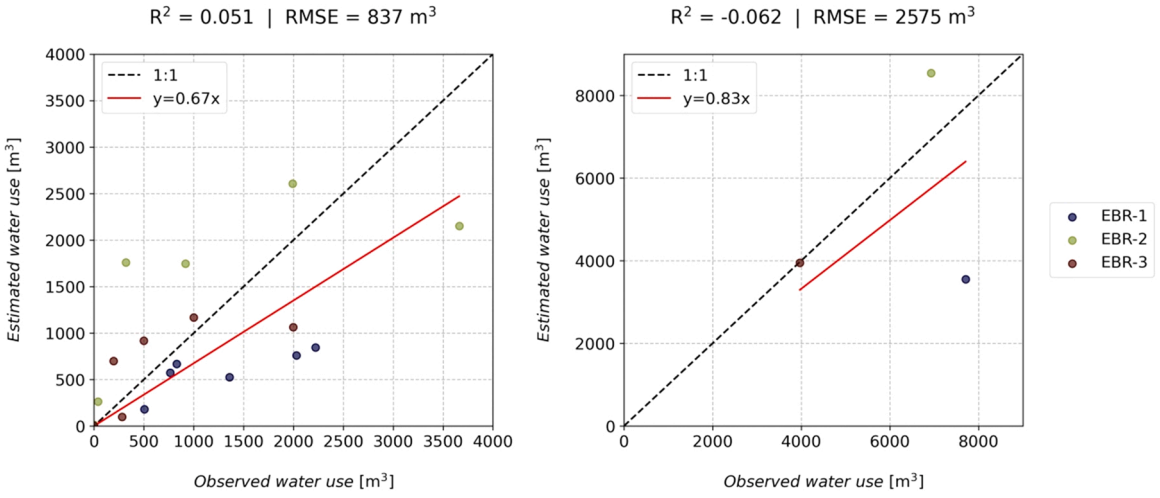

Fig. 7. The estimated water use compared to the observed water use for the Ebro study area at a monthly (left) and seasonal (right) time step.

from this study area. This shows that the temporal water use pattern in Namoi is not captured as well as for the other two study areas.

3.5. Temporal water use patterns

Our results show that, based on the KGE, the temporal water use patterns were not always accurately modeled. This is especially so for the Namoi area (Table 3). Fig. 10 demonstrates three different behaviors when comparing the estimated to the observed water uses in the Namoi area.

It can be observed in the figure that, for clusters that behave like NAM-7, the volumes are not correctly modeled (D_i = 76.0%). For the ones that act similarly as NAM-3, the cumulative water use is accurately estimated (D_i = 8.7%), but the timing is off. Lastly, the results of a few clusters, like NAM-11, show that the model is accurate in both the timing and cumulative amounts (KGE = 0.829; D_i = 2.6%). Although the main irrigation type in the area is furrow irrigation, which is assumed to be modeled less accurately, the temporal pattern should not have been affected, only the absolute estimated volumes applied to the field. The most likely cause for the general low KGE values is the location of the water meter itself. In arid climates, often reservoirs are constructed to store water for drier seasons (Biemans et al., 2011), which is also the case for the Namoi catchment (Pittock, 2016). In this area, the aim of installing the water meters is to control if a farmer withdraws the legal amount of ground or surface water, not to inform how much water is directly applied to the crops (Barma Water Resources et al., 2012). Therefore, there is a delay between the filling of the reservoir and the actual crop water consumption. Water is mostly pumped into the reservoirs during the winter, while irrigation is mostly applied during summer (Fuentes et al., 2021). This effect can be illustrated when comparing NAM-7 and NAM-11, the fields with the largest and smallest deviation in estimated and observed water use, respectively.

Fig. 11 shows the change in water surface area of the reservoirs connected to NAM-7 and NAM-11, which is derived from Sentinel-2

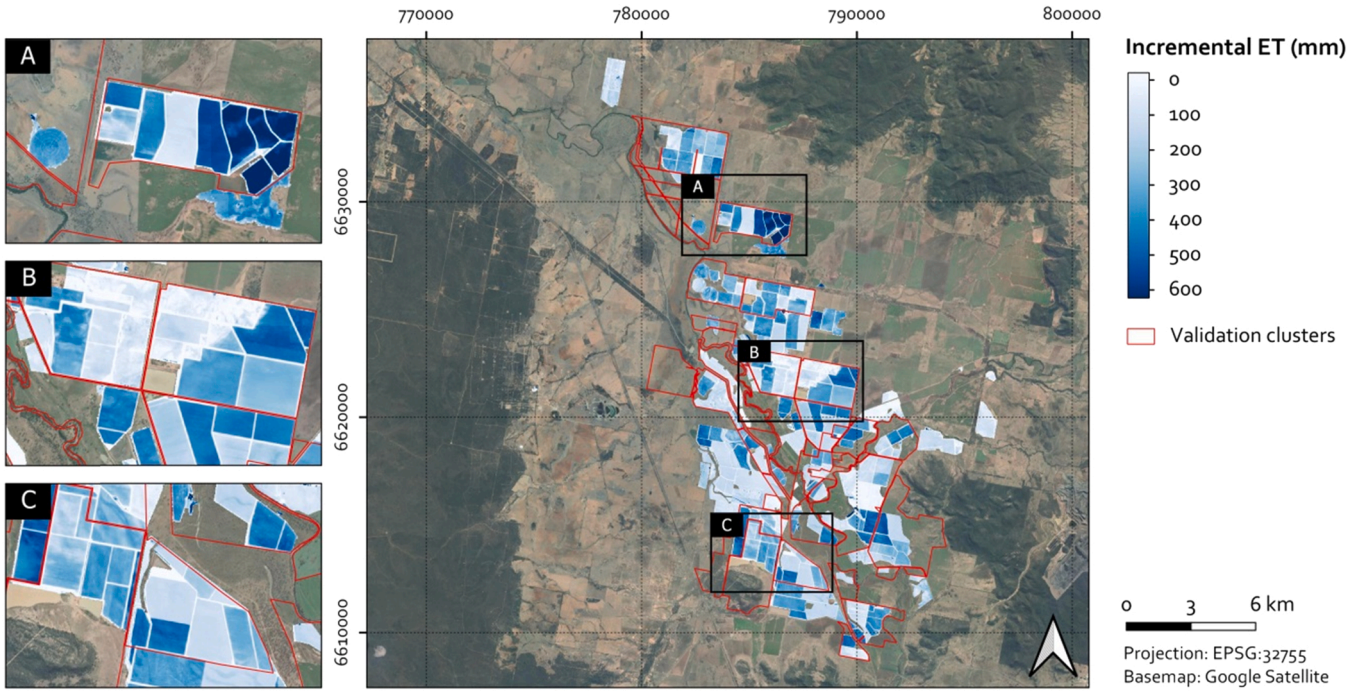

Fig. 8. The accumulated seasonal water use estimates (ET_{incr}) for the Namoi study area during the 2017–2018 season.

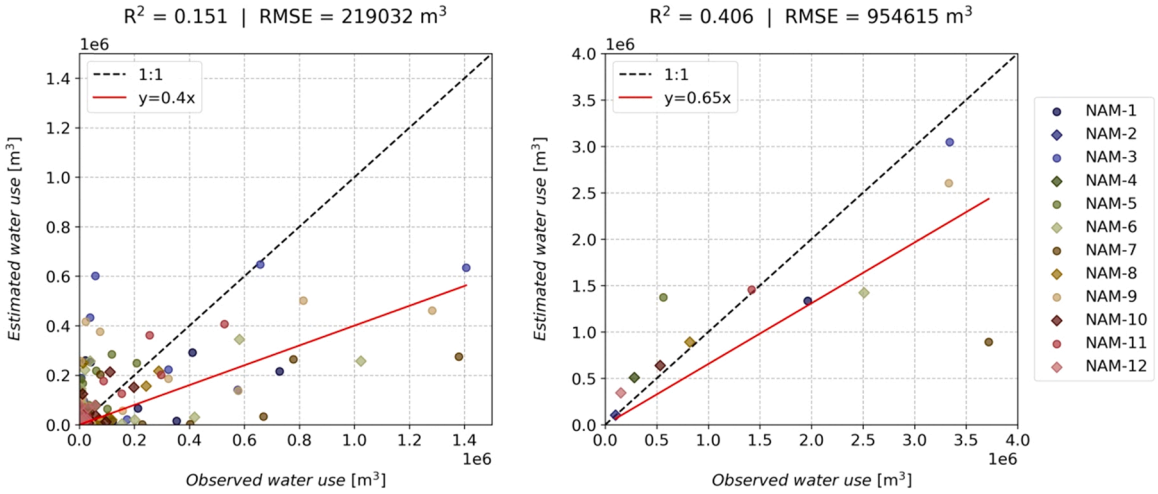

Fig. 9. The estimated water use compared to the observed water use for the Namoi study area at a monthly (left) and seasonal (right) time step.

Level-1 C observations using the Normalised Difference Water Index (NDWI) (McFeeters, 1996). NDWI pixels with a value larger than 0 are classified as water. There is a clear distinction between both clusters, with NAM-11 showing a relatively constant surface water area from winter till summer, while for NAM-7 the surface water area drops from 18 ha to less than 5 ha at the start of the season. In November, the reservoir of NAM-7 was rapidly filled and finally emptied with only 3 ha remaining at the beginning of July 2018. The reservoir of NAM-11 starts depleting in March 2018 and finally has a water surface area of 9 ha. Due to the analysis being done on Sentinel-2 Level-1 C images, atmospheric interference could have some effects on the surface water area observations, but the main differences between the two clusters are clear.

Based on Figs. 10 and 11, one could argue that more water is displaced throughout the season for NAM-7 compared to NAM-11. It is also evident that the reservoir of NAM-7 has been emptied and filled during the growing season, while the reservoir of NAM-11 remained more constant. For NAM-7, water is mostly displaced to fill the reservoir, not to directly irrigate the crops. For NAM-11, the pattern of the water surface area does not correlate well with the water meter observations, meaning that the water that is pumped into the reservoir is more directly used for irrigation. Excluding NAM-7 from the analysis shown in Fig. 9 would yield a seasonal R^2 of 0.793 instead of 0.406.

4. Discussion

In this research, we demonstrate the potential of the HSP algorithm to distinguish between the *ET* of natural and irrigated crops. In addition, we illustrate the capability of this model to calculate water use on a field level using high resolution (10 m) satellite data. However, the results also show limitations on the estimation of irrigation water use. For some fields, the estimates on monthly and on seasonal scales are not accurate. In this section, we provide a discussion on the used methods and their impact on the accuracy of the water use estimates. We also present a

Table 1
Statistics summary, i.e. seasonal estimated water use (Q_{est}), seasonal observed water use (Q_{obs}), the deviation between Q_{est} and Q_{obs} (D_i), Kling-Gupta efficiency (KGE), and root mean squared error (RMSE), of the monthly and seasonal water use estimations for the Hex Valley. For three fields, i.e. HEX-3, 6, and 9, only seasonal water use observations were available resulting in the KGE and RMSE not being calculated.

ID	Q_{est} m^3	Q_{obs} m^3	D_i %	KGE -	RMSE m^3
HEX-1	123,298	161,270	23.5	0.682	4,813
HEX-2	281,167	210,115	33.8	0.294	14,850
HEX-3	331,437	297,268	11.5	–	–
HEX-4	107,181	101,218	5.9	0.331	5,506
HEX-5	156,283	94,346	65.6	-0.120	10,050
HEX-6	300,922	398,198	24.4	–	–
HEX-7	59,261	38,965	52.1	0.444	2,975
HEX-8	38,626	42,966	10.1	0.534	2,062
HEX-9	175,643	189,522	7.3	–	–
HEX-10	76,447	52,059	46.8	0.185	4,477
HEX-11	147,601	104,888	40.7	0.348	7,684
HEX-12	100,720	155,234	35.1	0.341	9,450
HEX-13	296,370	280,450	5.7	0.539	14,081
HEX-14	242,617	220,190	10.2	0.558	12,794
HEX-15	128,565	104,189	23.4	0.479	6,461
Mean	171,076	163,392	4.7	0.385	7,934

Table 2
Statistics summary, i.e. seasonal estimated water use (Q_{est}), seasonal observed water use (Q_{obs}), the deviation between Q_{est} and Q_{obs} (D_i), Kling-Gupta efficiency (KGE), of the monthly and seasonal water use estimations for the Ebro study area.

ID	Q_{est} m^3	Q_{obs} m^3	D_i %	KGE -	RMSE m^3
EBR-1	3,553	7,710	53.9	0.112	854
EBR-2	8,542	6,927	23.3	0.543	955
EBR-3	3,950	3,971	0.5	0.561	477
Mean	5,348	6,203	13.8	0.405	762

Table 3
Statistics summary, i.e. seasonal estimated water use (Q_{est}), seasonal observed water use (Q_{obs}), the eviation between Q_{est} and Q_{obs} (D_i), Kling-Gupta efficiency (KGE), of the monthly and seasonal water use estimations for the Namoi study area.

ID	Q_{est} m^3	Q_{obs} m^3	D_i %	KGE -	RMSE m^3
NAM-1	1,336,500	1,962,000	31.9	0.115	213,074
NAM-2	105,930	100,000	5.9	-0.026	15,556
NAM-3	3,048,350	3,339,000	8.7	0.415	330,677
NAM-4	509,370	282,000	80.6	-0.364	54,796
NAM-5	1,372,400	562,600	143.9	-0.585	100,237
NAM-6	1,423,250	2,507,700	43.2	0.082	283,532
NAM-7	892,420	3,718,600	76.0	-0.111	420,651
NAM-8	892,030	818,700	9.0	0.484	89,367
NAM-9	2,602,950	3,332,000	21.9	0.262	332,167
NAM-10	640,080	533,000	20.1	0.559	55,375
NAM-11	1,456,770	1,420,100	2.6	0.829	65,169
NAM-12	345,780	150,300	130.1	-0.560	28,523
Mean	1,218,782	1,560,500	21.9	0.092	165,761

critical note on comparing in-situ observations with satellite-based models.

4.1. Model limitations

As with all types of modeling, compromises need to be made between computational efficiency and modeling accuracy. Since ETLook and the HSP algorithm are computationally expensive, multiple simplifications that might affect the quality of the final product have been applied.

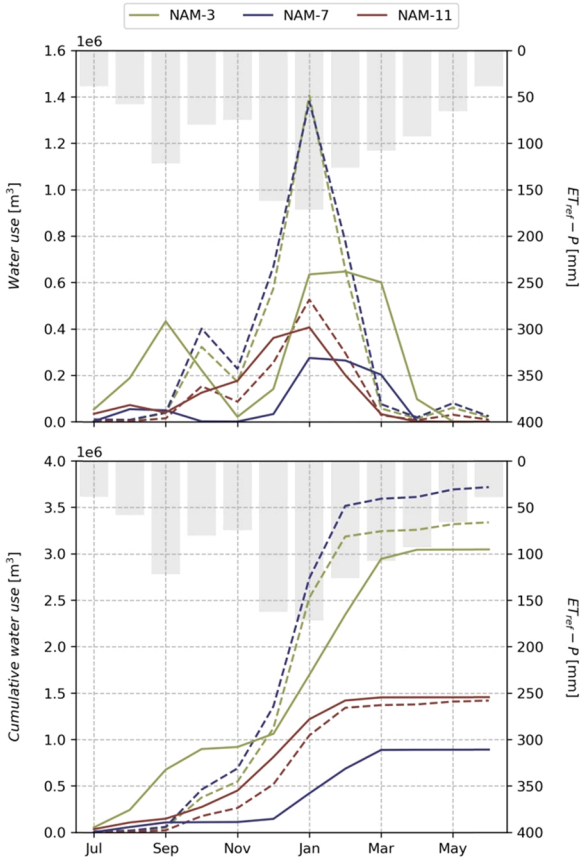

Fig. 10. Comparison between the estimated (solid lines) and observed (dashed lines) water use for three clusters of fields in the Namoi study area, at a monthly interval. The top figure shows the monthly water use and the bottom the monthly cumulative water use. The second y-axis shows a bar plot with the difference between the reference evapotranspiration (ET_{ref}) and the precipitation (P).

4.1.1. Evapotranspiration modeling

For all the study areas, the ETLook algorithm was run to produce daily evapotranspiration estimates. These were converted to monthly and seasonal values to compare with equivalent water use estimates.

Since ETLook calculates E and T based on a modified Penman-Monteith equation, it shares the same limitations. The main one is the fact that the stomatal resistance and soil resistance are hard to quantify. Regarding the stomatal resistance, there is a dependence on land use. Each class is assigned a defined value for the canopy resistance. So the quality of the transpiration estimate is dependent on the quality of the land use classification. In its turn, the soil resistance is a function of the topsoil moisture content. So any uncertainty in the topsoil moisture estimations is propagated to the calculation of the evaporation (Subedi and Chávez, 2015).

While some input data for ETLook is available daily (meteorological inputs), others are less frequent (NDVI, albedo, and land surface temperature) and subject to cloud cover. In cloudless conditions, we can predict that every pixel would be seen by either Sentinel 2 or Landsat 8 about 90 times per year. However, that is hardly the case. The impact of this on the HSP results is hard to predict. For the irrigated pixels, on the one hand, it is expected that the variation of optical inputs is well captured, as farmers would irrigate more during drier, cloudless conditions. For the natural rain-fed vegetation, on the other hand, important phenological information might be missed during the cloudy periods.

In addition, the source of the daily meteorological data interferes with the accuracy of both ETlook and HSP algorithms. For one study area, the Ebro basin, the data came exclusively from climate models. In

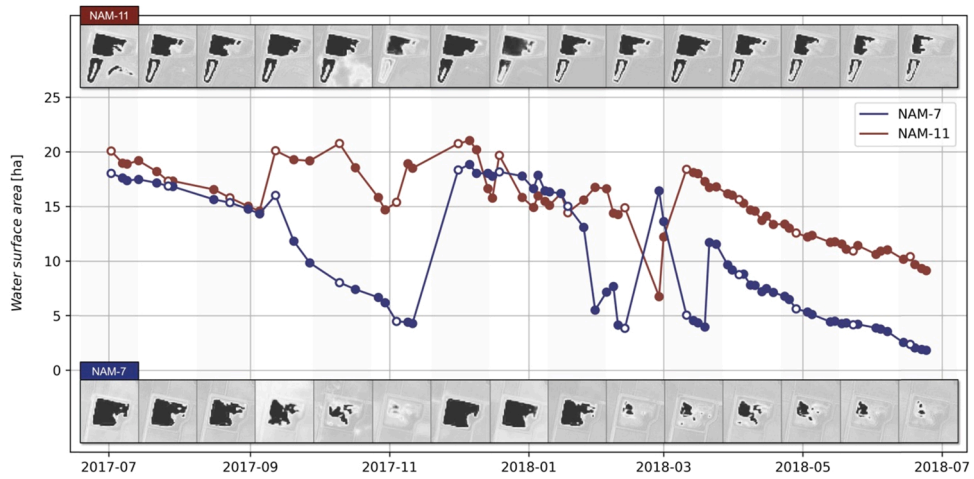

Fig. 11. The water surface area time series of the reservoirs of NAM-7 (blue) and NAM-11 (red) derived using the Normalised Difference Water Index (NDWI) acquired from Sentinel-2 Level-1 C satellite observations. On the top (NAM-11) and the bottom (NAM-7) of the plot, a couple of NDWI images of the two reservoirs are shown as an example, with dark pixels indicating water surfaces. The hollow points correspond to the timing of the NDWI images shown in the figure.

the other two regions, modeled data was only employed when locally measured data was not available.

4.1.2. Definition of hydrological similarity

Currently, the similarity is based on the slope, aspect, TWI, clay content, silt content, and sand content. However, these inputs are all considered of equal importance when calculating the similarity. One could argue that some of these inputs are more important than others for explaining the hydrogeomorphological differences between pixels. Future studies should include decisions on the weight of each static input when calculating the similarity score.

Furthermore, additional soil characteristics from the SoilGrids database could be included (Hengl et al., 2017). However, due to the limited search radius of the algorithm (a few kilometers), it is not expected that these characteristics will show a significant difference, without showing a significant change in sand, silt, and clay content.

Besides the current static inputs, additional periodic datasets could be obtained to assess the hydrological similarity. Examples of such datasets could be soil moisture estimates (Massari et al., 2021) and rooting depth models (de Wit et al., 2019). Soil moisture datasets give insight into the spatiotemporal variability of the water availability, where the currently used TWI only shows the spatial distribution based on topography. Rooting depth models can be implemented to more accurately calculate the Total Available Water (*TAW*) parameter.

4.1.3. Availability of natural pixels

The HSP algorithm depends on the availability of natural pixels. However, some agricultural schemes might be so extensive that it is difficult to find a suitable subset of natural pixels. This is evident for the Ebro study area, as shown in Fig. 12.

The study area in the Ebro basin is effectively one entire irrigation scheme with limited natural areas, while the Hex Valley is fully surrounded by natural pixels. For the Hex Valley, the maximum average distance to the subset of natural pixels is about 1 km, while for the Ebro study area, this value can go up to 3 km for some pixels. This increase in distance induces uncertainties when comparing the *ET* of native

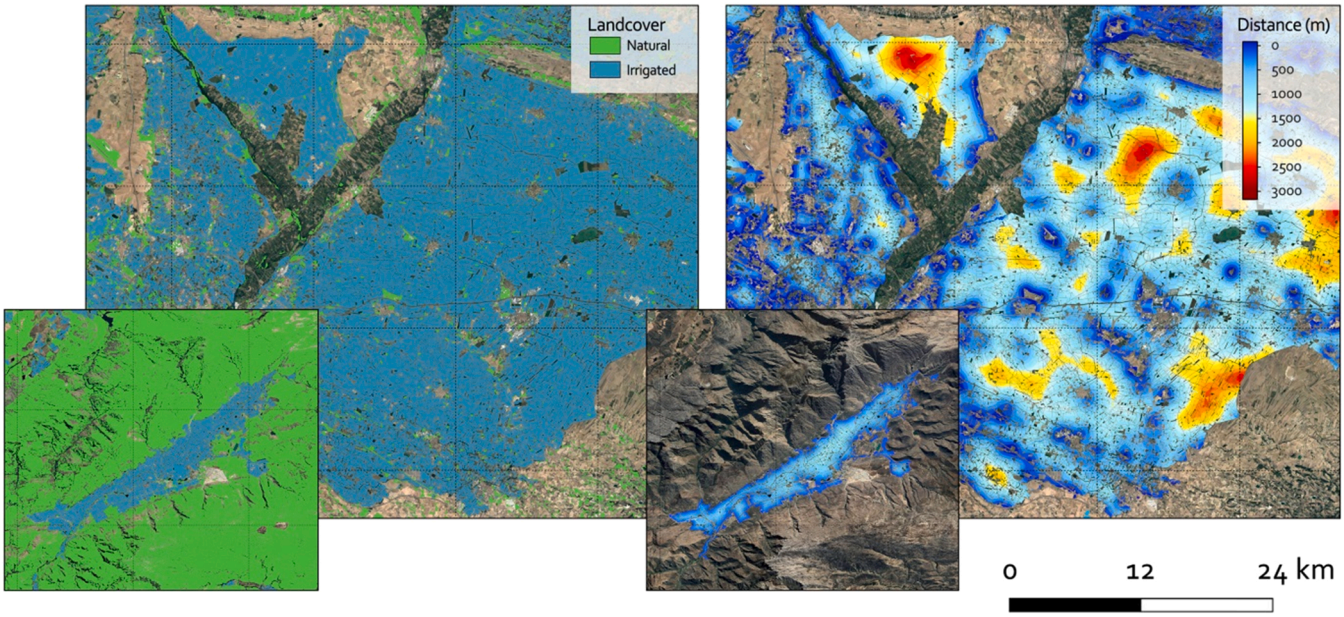

Fig. 12. Comparison between the amount of natural and irrigated agricultural pixels (left); and between the average distance to the subset of natural pixels (right) for the Ebro (large images) and Hex Valley (small images) study areas.

vegetation and irrigated agriculture as it might violate the concept that all the other terms in the water balance (Eq. (1)) must be similar. Thus, for areas like the Ebro basin, alternative approaches should be considered.

In addition, as mentioned by Van Eekelen et al. (2015), all land cover classification maps have their inaccuracies, which will affect the water use estimates. If, for example, a built-up area is classified as natural vegetation, the incremental *ET* and the water use will be overestimated. To decrease the impact of falsely classified natural areas, the size of the subset of similar pixels can be increased. However, this impacts the computational efficiency and increases the mean distance of the subset, affecting its hydrological similarity. A second option is to exclude natural pixels which do not show any vegetation development throughout the season, for example, by excluding pixels with a maximum seasonal NDVI of 0.3.

Another solution could be to compare non-irrigated agricultural pixels to irrigated ones. That would solve the issue of having limited access to natural pixels. On the other hand, current land cover maps are not reliable enough to assume that non-irrigated plots are indeed not irrigated. Such maps are usually not updated every year. Furthermore, annual crops often rotate every season, resulting in changing irrigation practices. It raises the need for an annually or seasonally updated irrigated area map, which will be the focus of future studies. Having an up-to-date and accurate irrigated area map would also improve the accuracy of the water use estimates because the ET_{incr} is only calculated for areas that are classified as irrigated agriculture. If the current land cover maps underestimate the irrigated area, the water use is also underestimated.

4.2. Validity of comparison with water meters

Besides the known limitations of the models, directly comparing satellite observations with in-situ measurements is always challenging (Loew et al., 2017). A water meter is not a standardized instrument, and each system has its inaccuracies (Boman and Shukla, 2009; Dobriyal et al., 2017; Su et al., 2021). Hightech agricultural systems might be equipped with fully automated and efficient irrigation equipment which accurately measure the water use. Nevertheless, most schemes are inefficient and depend on manual labor. Furrow irrigation is among the least efficient irrigation types, with an overall efficiency of 45%, whereas for drip irrigation, considered the most efficient type, the overall efficiency rises to 90% (Savva and Frenken, 2002). An added challenge is that, while water meters account for all the water applied to the field, only the irrigated water consumed by the crop is observed in our satellite-based measurements. Intermediate losses, such as open water evaporation, percolation, runoff, and leakages are not monitored. Thus, in its current form, satellite-based water use estimates should be more comparable to drip irrigation systems and less related to poorly performing irrigation types such as furrow or sprinkler irrigation.

It is also known that water meters are not always installed to monitor the water that is directly applied to the field, but rather to observe how much water is taken from the environment and stored in reservoirs (Fuentes et al., 2021). Fig. 11 illustrates that this is presumably the reason for the mismatch in the temporal patterns of the estimated and observed water use (Table 3). It also shows that for a reservoir that fluctuates a lot in the amount of water stored (NAM-7), the seasonal accuracy of the satellite based water use estimates decreased significantly. It is therefore crucial that when comparing water meter data to remote sensing based water use estimates, the water meter is directly coupled to the irrigation system, instead of being connected to an intermediate reservoir.

5. Conclusions

In this study, we demonstrated that, depending on the study area, it is possible to accurately estimate the monthly and seasonal water use of irrigated agriculture using high resolution (10 m) remote sensing-based evapotranspiration estimates and the newly introduced HSP algorithm.

The Hex Valley (South Africa) study area yielded the best results, with a seasonal R^2 of 0.780. For the Ebro (Spain) study area, limited validation data was available, but in general, the results were less accurate than for the Hex Valley. The limited amount of natural pixels in the Ebro study area (Fig. 12) also made the execution of the HSP algorithm more challenging. The results of the Namoi (Australia) study area were accurate at seasonal scale ($R^2 = 0.793$; excluding NAM-7) but showed timing issues on a monthly basis due to the water meters being connected to large reservoirs instead of being directly connected to the irrigation systems.

A use case of the proposed method, which we already implemented in some South African Catchment Management Agencies, is to compare our water use estimates with predefined water allocations. This enables local water authorities to identify big water consumers and to enforce local withdrawal laws in times of drought. Further research will implement an annual irrigated area map to improve the accuracy of the model, and the HSP algorithm will subsequently be tested while comparing irrigated to non-irrigated crops for areas that have limited availability of natural pixels.

Funding

This work was supported by the European Commission's Horizon 2020 Research and Innovation Programme through the WaterSENSE Project [grant number 870344], and by the European Space Agency (ESA) through the IRRIGATION+ [grant number 4000129870/20/I-NB] and CCN OWASIS projects [grant number 4000118604/16/NL/US].

Declaration of Competing Interest

The authors declare the following financial interests/personal relationships which may be considered as potential competing interests: Joost Brombacher reports financial support was provided by the European Commission. Joost Brombacher reports financial support was provided by the European Space Agency.

Acknowledgments

We would like to thank the Hex Valley Water Users Association, IRTA, and Water Technology for providing the water meter observation data which was used for the validation of our results.

References

Arshad, M., Guillaume, J.H.A., Ross, A., 2014. Assessing the feasibility of managed aquifer recharge for irrigation under uncertainty. Water 6, 2748–2769.

Barma Water Resources, Thurtell, L., Wettin, P., 2012, Environmental Water Delivery: Namoi River, Prepared for Commonwealth Environmental Water, Department of Sustainability, Environment, Water, Population and Communities, Canberra. https://www.awe.gov.au/sites/default/files/documents/ewater-delivery-namoi-river.pdf (accessed 4 March 2022).

Bastiaanssen, W.G.M., Cheema, M.J.M., Immerzeel, W.W., Miltenburg, I.J., Pelgrum, H., 2012. Surface energy balance and actual evapotranspiration of the transboundary Indus Basin estimated from satellite measurements and the ETLook model. Water Resour. Res. 48, 1–16. https://doi.org/10.1029/2011WR010482.

Bastiaanssen, W.G.M., Pelgrum, H., Wang, J., Ma, Y., Moreno, J.F., Roerink, G.J., van der Wal, T., 1998. A remote sensing surface energy balance algorithm for land (SEBAL), Part 1: Formulation. J. Hydrol. 212–213, 198–212. https://doi.org/10.1016/S0022-1694(98)00254-6.

Beven, K.J., Kirkby, M.J., 1979. A physically based, variable contributing area model of basin hydrology. Hydrol. Sci. J. 24, 43–69. https://doi.org/10.1080/02626667909491834.

Biemans, H., Haddeland, I., Kabat, P., Ludwig, F., Hutjes, R.W.A., Heinke, J., Von Bloh, W., Gerten, D., 2011. Impact of reservoirs on river discharge and irrigation water supply during the 20th century. Water Resour. Res 47. https://doi.org/10.1029/2009WR008929.

Blatchford, M.L., Mannaerts, C.M., Njuki, S.M., Nouri, H., Zeng, Y., Pelgrum, H., Wonink, S., Karimi, P., 2020. Evaluation of WaPOR V2 evapotranspiration products across Africa. Hydrol. Sci. J. 34, 3200–3221. https://doi.org/10.1002/hyp.13791.

Boman, B., Shukla, S., 2009. Water Measurement for Agricultural Irrigation and Drainage Systems, Agricultural and Biological Engineering Department. Florida Cooperative Extension Service. University of Florida, accessed 4 March 2022. ⟨https://edis.ifas.ufl.edu/pdf/CH/CH15300.pdf⟩.

Bretreger, D., Yeo, I.Y., Hancock, G., Willgoose, G., 2020. Monitoring irrigation using landsat observations and climate data over regional scales in the Murray-Darling Basin. J. Hydrol. 590. https://doi.org/10.1016/j.jhydrol.2020.125356.

Brocca, L., Tarpanelli, A., Filippucci, P., Dorigo, W., Zaussinger, F., Gruber, A., Fernández-Prieto, D., 2018. How much water is used for irrigation? A new approach exploiting coarse resolution satellite soil moisture products. Int. J. Appl. Earth Obs. Geoinf. 73, 752–766. https://doi.org/10.1016/j.jag.2018.08.023.

Bureau of Meteorology, 2021, Climate statistics for Australian locations: Summary statistics Narrabri West Post Office [WWW Document]. http://www.bom.gov.au/climate/averages/tables/cw_053030.shtml (accessed 4 June 2021).

Chai, T., Draxler, R.R., 2014. Root mean square error (RMSE) or mean absolute error (MAE)? -Arguments against avoiding RMSE in the literature. Geosci. Model Dev. 7, 1247–1250. https://doi.org/10.5194/gmd-7-1247-2014.

Conrad, O., Bechtel, B., Bock, M., Dietrich, H., Fischer, E., Gerlitz, L., Wehberg, J., Wichmann, V., Böhner, J., 2015. System for Automated Geoscientific Analyses (SAGA) v. 2.1.4. Geosci. Model Dev. 8, 1991–2007. https://doi.org/10.5194/gmd-8-1991-2015.

Dari, J., Brocca, L., Quintana-Seguí, P., Escorihuela, M.J., Stefan, V., Morbidelli, R., 2020. Exploiting high-resolution remote sensing soil moisture to estimate irrigation water amounts over a Mediterranean region. Remote Sens 12. https://doi.org/10.3390/RS12162593.

de Wit, A., Boogaard, H., Fumagalli, D., Janssen, S., Knapen, R., van Kraalingen, D., Supit, I., van der Wijngaart, R., van Diepen, K., 2019. 25 years of the WOFOST cropping systems model. Agric. Syst. 168, 154–167. https://doi.org/10.1016/j.agsy.2018.06.018.

Dobriyal, P., Badola, R., Tuboi, C., Hussain, S.A., 2017. A review of methods for monitoring streamflow for sustainable water resource management. Appl. Water Sci. 7, 2617–2628. https://doi.org/10.1007/s13201-016-0488-y.

DPIE, 2020, New South Wales Landuse 2017 v1.2 [WWW Document]. https://datasets.seed.nsw.gov.au/dataset/nsw-landuse-2017-v1p2-f0ed (accessed 28 July 2021).

ESA, 2021, How ESA helps South Africa share water Fairly [WWW Document]. ESA Telecommun. Integr. Appl. https://www.esa.int/Applications/Telecommunications_Integrated_Applications/How_ESA_helps_South_Africa_share_water_fairly (accessed 21 July 2021).

ESA, 2012, Sentinel-2 ESA's Optical High-Resolution Mission for GMES Operational Services. ESA Spec. Publ. SP-1322/2, 1–70.

ESA, 1999, Meteosat Second Generation - The Satellite Development, ESA Publications Division. https://earth.esa.int/eogateway/documents/20142/37627/Meteosat-Second-Generation-The-Satellite-Development.pdf (accessed 4 March 2022).

FAO, 2011, The State of the World's Land and Water Resources (SOLAW) - Managing Systems at Risk. Rome/London. https://www.fao.org/3/i1688e/i1688e.pdf (accessed 4 March 2022).

Foster, T., Mieno, T., Brozović, N., 2020. Satellite-based monitoring of irrigation water use: assessing measurement errors and their implications for agricultural water management policy. Water Resour. Res 56. https://doi.org/10.1029/2020WR028378.

Fuentes, I., Scalzo, R., Vervoort, R.W., 2021. Volume and uncertainty estimates of on-farm reservoirs using surface reflectance and LiDAR data. Environ. Model. Softw. 143. https://doi.org/10.1016/j.envsoft.2021.105095.

Gao, Q., Zribi, M., Escorihuela, M.J., Baghdadi, N., Segui, P.Q., 2018. Irrigation mapping using Sentinel-1 time series at field scale. Remote Sens 10. https://doi.org/10.3390/rs10091495.

Gupta, H.V., Kling, H., Yilmaz, K.K., Martinez, G.F., 2009. Decomposition of the mean squared error and NSE performance criteria: Implications for improving hydrological modelling. J. Hydrol. 377, 80–91. https://doi.org/10.1016/j.jhydrol.2009.08.003.

Hengl, T., 2007, A Practical Guide to Geostatistical Mapping of Environmental Variables, EUR 22904 EN. Luxembourg (Luxembourg): Office for Official Publications of the European Communities. https://doi.org/10.1016/0277–9390(86)90082–8.

Hengl, T., de Jesus, Mendes, Heuvelink, J., Ruiperez Gonzalez, G.B.M., Kilibarda, M., Blagotić, A, M., 2017. SoilGrids250m: Global gridded soil information based on machine learning. PLoS One 12. https://doi.org/10.1371/journal.pone.0169748.

Hennig, T.A., Kretsch, J.L., Pessagno, C.J., Salamonowicz, P.H., Stein, W.L., 2007. The shuttle radar topography mission. Rev. Geophys 42. https://doi.org/10.1007/3-540-44818-7_11.

Herron, N., Peeters, L., Crosbie, R., Marvanek, S., Pagendam, D., Ramage, A., Rachakonda, P., Wilkins, A., 2018, Groundwater numerical modelling for the Hunter subregion, Product 2.6.2 for the Namoi subregion from the Northern Inland Catchments Bioregional Assessment. Department of the Environment and Energy, Bureau of Meteorology, CSIRO and Geoscience Australia, Australia. https://www.bioregionalassessments.gov.au/sites/default/files/ba-nsb-hun-262-gwmodelling-20180304-v2.pdf (accessed 4 March 2022).

IPCC, 2021, Summary for Policymakers, Climate Change 2021: The Physical Science Basis. Contribution of Working Group I to the Sixth Assessment Report of the Intergovernmental Panel on Climate Change. [Masson-Delmotte, V., P. Zhai, A. Pirani, S. L. Connors, C. Péan, S. Berger, N. Caud, Y. Chen, L. Goldfarb, M. I. Gomis, M. Huang, K. Leitzell, E. Lonnoy, J.B.R. Matthews, T. K. Maycock, T. Waterfield, O. Yelekçi, R. Yu and B. Zhou (eds.)], Cambridge University Press. https://www.ipcc.ch/report/ar6/wg1/downloads/report/IPCC_AR6_WGI_SPM_final.pdf (accessed 4 March 2022).

Jägermeyr, J., Gerten, D., Heinke, J., Schaphoff, S., Kummu, M., Lucht, W., 2015. Water savings potentials of irrigation systems: Global simulation of processes and linkages. Hydrol. Earth Syst. Sci. 19, 3073–3091. https://doi.org/10.5194/hess-19-3073-2015.

Jalilvand, E., Tajrishy, M., Ghazi Zadeh Hashemi, S.A., Brocca, L., 2019. Quantification of irrigation water using remote sensing of soil moisture in a semi-arid region. Remote Sens. Environ. 231, 111226 https://doi.org/10.1016/j.rse.2019.111226.

Japan Meteorological Agency, 2015, Himawari-8/9 Standard Data User's Guide Version 1.2. https://www.data.jma.go.jp/mscweb/en/himawari89/space_segment/hsd_sample/HS_D_users_guide_en_v12.pdf (accessed 4 March 2022).

Jovanovic, N., Israel, S., 2012, Critical Review of Methods for the Estimation of Actual Evapotranspiration in Hydrological Models, in: Evapotranspiration - Remote Sensing and Modeling. https://doi.org/10.5772/21279.

Knoben, W.J.M., Freer, J.E., Woods, R.A., 2019. Technical note: Inherent benchmark or not? Comparing Nash-Sutcliffe and Kling-Gupta efficiency scores. Hydrol. Earth Syst. Sci. 23, 4323–4331. https://doi.org/10.5194/hess-23-4323-2019.

Koch, J., Zhang, W., Martinsen, G., He, X., Stisen, S., 2020. Estimating net irrigation across the North China Plain through dual modeling of evapotranspiration. Water Resour. Res 56. https://doi.org/10.1029/2020WR027413.

Koech, R., Langat, P., 2018. Improving irrigation water use efficiency: A review of advances, challenges and opportunities in the Australian context. Water 10. https://doi.org/10.3390/w10121771.

Lam, S.K., Pitrou, A., Seibert, S., 2015, Numba: a LLVM-based Python JIT compiler. LLVM '15 Proc. Second Work. LLVM Compil. Infrastruct. HPC 1–6.

Lesiv, M., Laso Bayas, J.C., See, L., Duerauer, M., Dahlia, D., Durando, N., Hazarika, R., Kumar Sahariah, P., Vakolyuk, M., Blyshchyk, V., Bilous, A., Perez-Hoyos, A., Gengler, S., Prestele, R., Bilous, S., Akhtar, I. ul H., Singha, K., Choudhury, S.B., Chetri, T., Malek, Ž., Bungnamei, K., Saikia, A., Sahariah, D., Narzary, W., Danylo, O., Sturn, T., Karner, M., McCallum, I., Schepaschenko, D., Moltchanova, E., Fraisl, D., Moorthy, I., Fritz, S., 2019. Estimating the global distribution of field size using crowdsourcing. Glob. Chang. Biol. 25, 174–186. https://doi.org/10.1111/gcb.14492.

Linstead, C., 2018. The contribution of improvements in irrigation efficiency to environmental flows. Front. Environ. Sci. 6, 1–6. https://doi.org/10.3389/fenvs.2018.00048.

Loew, A., Bell, W., Brocca, L., Bulgin, C.E., Burdanowitz, J., Calbet, X., Donner, R.V., Ghent, D., Gruber, A., Kaminski, T., Kinzel, J., Klepp, C., Lambert, J.C., Schaepman-Strub, G., Schröder, M., Verhoelst, T., 2017. Validation practices for satellite-based Earth observation data across communities. Rev. Geophys. 55, 779–817. https://doi.org/10.1002/2017RG000562.

Massari, C., Modanesi, S., Dari, J., Gruber, A., De Lannoy, G.J.M., Girotto, M., Quintana-Seguí, P., Le Page, M., Jarlan, L., Zribi, M., Ouaadi, N., Vreugdenhil, M., Zappa, L., Dorigo, W., Wagner, W., Brombacher, J., Pelgrum, H., Jaquot, P., Freeman, V., Volden, E., Prieto, D.F., Tarpanelli, A., Barbetta, S., Brocca, L., 2021. A review of irrigation information retrievals from space and their utility for users. Remote Sens 13, 1–26. https://doi.org/10.3390/rs13204112.

McFeeters, S.K., 1996. The use of the Normalized Difference Water Index (NDWI) in the delineation of open water features. Int. J. Remote Sens. 17, 1425–1432. https://doi.org/10.1080/01431169608948714.

Milano, M., Ruelland, D., Dezetter, A., Fabre, J., Ardoin-Bardin, S., Servat, E., 2013. Modeling the current and future capacity of water resources to meet water demands in the Ebro basin. J. Hydrol. 500, 114–126. https://doi.org/10.1016/j.jhydrol.2013.07.010.

Moene, A., Dam, J., 2014. Transport in the Atmosphere-Vegetation-Soil Continuum. Cambridge University Press, Cambridge.

Mohamed, J., Ali, S., 2006, Development and comparative analysis of pedotransfer functions for predicting soil water characteristic content for Tunisian soil. Proc. 7th Ed. TJASSST 170–178.

Muñoz-Sabater, J., 2019, ERA5-Land monthly averaged data from 1981 to present. Copernicus Climate Change Service (C3S) Climate Data Store (CDS) [WWW Document]. https://doi.org/10.24381/cds.68d2bb3.

Ncube, B., 2018, Approaches for emerging farmer participation in water resource management: the case of the Breede-Gouritz Catchment Management Agency (BGCMA), Western Cape: report to the Water Research Commission. http://www.wrc.org.za/wp-content/uploads/mdocs/2310–1-171.pdf (accessed 4 March 2022).

Noh, S.J., An, H., Kim, S., Kim, H., 2015. Simulation of soil moisture on a hillslope using multiple hydrologic models in comparison to field measurements. J. Hydrol. 523, 342–355. https://doi.org/10.1016/j.jhydrol.2015.01.047.

Pedregosa, F., Varoquaux, G., Gramfort, A., Michel, V., Thirion, B., Grisel, O., Blondel, M., Prettenhofer, P., Weiss, R., Dubourg, V., Vanderplas, J., Passos, A., Cournapeau, D., Brucher, M., Perrot, M., Duchesnay, E., 2011. Scikit-learn: machine learning in python. J. Mach. Learn. Res 12, 2825–2830. https://doi.org/10.1289/EHP4713.

Peng, J., Albergel, C., Balenzano, A., Brocca, L., Cartus, O., Cosh, M.H., Crow, W.T., Dabrowska-Zielinska, K., Dadson, S., Davidson, M.W.J., de Rosnay, P., Dorigo, W., Gruber, A., Hagemann, S., Hirschi, M., Kerr, Y.H., Lovergine, F., Mahecha, M.D., Marzahn, P., Mattia, F., Musial, J.P., Preuschmann, S., Reichle, R.H., Satalino, G., Silgram, M., van Bodegom, P.M., Verhoest, N.E.C., Wagner, W., Walker, J.P., Wegmüller, U., Loew, A., 2021. A roadmap for high-resolution satellite soil moisture applications – confronting product characteristics with user requirements. Remote Sens. Environ. 252, 112162 https://doi.org/10.1016/j.rse.2020.112162.

Perry, C., 2017. Does improved irrigation technology save water? A review of the evidence. Food and agriculture organization of the United Nations,, Cairo. ⟨https://www.fao.org/3/I7090EN/i7090en.pdf⟩.

Pittock, J., 2016. The Murray-Darling basin: climate change, infrastructure, and water. Increasing Resilience to Climate Variability and Change. Springer,, pp. 41–59. https://doi.org/10.1007/978-981-10-1914-2.

Rahman, H., Dedieu, G., 1994. SMAC: A simplified method for the atmospheric correction of satellite measurements in the solar spectrum. Int. J. Remote Sens 15, 123–143. https://doi.org/10.1080/01431169408954055.

Richter, R., Kellenberger, T., Kaufmann, H., 2009. Comparison of topographic correction methods. Remote Sens 1, 184–196. https://doi.org/10.3390/rs1030184.

Rienecker, M.M., Suarez, M.J., Todling, R., Bacmeister, J., Takacs, L., Liu, H.-C., Gu, W., Sienkiewicz, M., Koster, R.D., Gelaro, R., Nielsen, J.E., 2008, The GEOS-5 Data Assimilation System - Documentation of Versions 5.0. 1, 5.1. 0, and 5.2. 0, Technical Report Series on Global Modeling and Data Assimilation. https://gmao.gsfc.nasa.gov/pubs/docs/Rienecker369.pdf (accessed 4 March 2022).

Roger, J.C., Vermote, E.F., Devadiga, S., Ray, J.P., 2017, Suomi-NPP VIIRS Surface Reflectance User's Guide. Version 1.6. https://lpdaac.usgs.gov/documents/124/VNP09_User_Guide_V1.6.pdf (accessed 4 March 2022).

Romaguera, M., Krol, M.S., Suhyb Salama, M., Hoekstra, A.Y., Su, Z., 2012. Determining irrigated areas and quantifying blue water use in Europe using remote sensing Meteosat Second Generation (MSG) products and Global Land Data Assimilation System (GLDAS) Data. Photogramm. Eng. Remote Sens. 78, 861–873. https://doi.org/10.14358/PERS.78.8.861.

Rouf, T., Mei, Y., Maggioni, V., Houser, P., Noonan, M., 2020. A physically based atmospheric variables downscaling technique. J. Hydrometeorol. 21, 93–108. https://doi.org/10.1175/JHM-D-19-0109.1.

Roy, D.P., Lewis, P., Schaaf, C.B., Devadiga, S., Boschetti, L., 2006. The global impact of clouds on the production of MODIS bidirectional reflectance model-based composites for terrestrial monitoring. IEEE Geosci. Remote Sens. Lett. 3, 452–456. https://doi.org/10.1109/LGRS.2006.875433.

Savva, A.P., Frenken, K., 2002. Crop Water Requirements and Irrigation Scheduling: Irrigation Manual. Module 4, Harare. ⟨https://www.fao.org/3/ai593e/ai593e.pdf⟩. accessed 4 March 2022.

Seabold, S., Perktold, J., 2010, Statsmodels: Econometric and Statistical Modeling with Python. Proc. 9th Python Sci. Conf. 92–96. https://doi.org/10.25080/majora-92bf1922–011.

SIOSE, 2018, Sistema de Información de Ocupación del Suelo en España: Documento técnico SIOSE 2014. https://www.siose.es/SIOSEtheme-theme/documentos/pdf/Doc_tec_SIOSE2014_v1.pdf (accessed 4 March 2022).

Sishodia, R.P., Ray, R.L., Singh, S.K., 2020. Applications of remote sensing in precision agriculture: A review. Remote Sens 12, 1–31. https://doi.org/10.3390/rs12193136.

Sørensen, R., Zinko, U., Seibert, J., 2006. On the calculation of the topographic wetness index: evaluation of different methods based on field observations. Hydrol. Earth Syst. Sci. 10, 101–112. https://doi.org/10.5194/hess-10-101-2006.

Su, M., Jiao, X., Li, J., Wu, S., Wu, T., 2021. Accuracy and reliability analysis of pipe irrigation metering device for sandy water source. Water 13, 1–14. https://doi.org/10.3390/w13070947.

Subedi, A., Chávez, J.L., 2015. Crop Evapotranspiration (ET) Estimation Models: A Review and Discussion of the Applicability and Limitations of ET Methods. J. Agric. Sci. 7. https://doi.org/10.5539/jas.v7n6p50.

Tazekrit, I., Benslimane, M., Simonneaux, V., Hartani, T., Hamimed, A., 2018. Estimation of irrigation water pumping by remote sensing: Application of the SAMIR model to citrus under mediterranean climate conditions. Rev. Bras. Meteorol. 33, 391–400. https://doi.org/10.1590/0102-7786333016.

Thompson, M., 2019, South African National Land-Cover 2018: Report & Accuracy Assessment. https://sfiler.environment.gov.za:8443/ssf/s/readFile/folderEntry/40903/8afbc1c77a484088017a4dddf3f3003f/1624802400000/last/SA_NLC_2020_Accuracy_Assessment_Report.zip.

Thoreson, B., Clark, B., Soppe, R., Keller, A., Bastiaanssen, W., Eckhardt, J., 2009. Comparison of evapotranspiration estimates from remote sensing (SEBAL), water balance, and crop coefficient approaches. World Environ. Water Resour. Congr. 2009, 1–15. https://doi.org/10.1061/41036(342)437.

U.S. Geological Survey, 2015, Landsat - Earth observation satellites, U.S. Geological Survey. https://doi.org/10.3133/fs20153081.

Van Eekelen, M.W., Bastiaanssen, W.G.M., Jarmain, C., Jackson, B., Ferreira, F., Van der Zaag, P., Saraiva Okello, A., Bosch, J., Dye, P., Bastidas-Obando, E., Dost, R.J.J., Luxemburg, W.M.J., 2015. A novel approach to estimate direct and indirect water withdrawals from satellite measurements: A case study from the Incomati basin. Agric. Ecosyst. Environ. 200, 126–142. https://doi.org/10.1016/j.agee.2014.10.023.

World Economic Forum, 2021, The Global Risks Report 2021: 16th Edition. http://www3.weforum.org/docs/WEF_The_Global_Risks_Report_2021.pdf (accessed 4 March 2022).

Yang, Y., Guan, H., Long, D., Liu, B., Qin, G., Qin, J., Batelaan, O., 2015. Estimation of surface soil moisture from thermal infrared remote sensing using an improved trapezoid method. Remote Sens 7, 8250–8270. https://doi.org/10.3390/rs70708250.

Zappa, L., Schlaffer, S., Bauer-Marschallinger, B., Nendel, C., Zimmerman, B., Dorigo, W., 2021. Detection and quantification of irrigation water amounts at 500 m using sentinel-1 surface soil moisture. Remote Sens 13, 1–20. https://doi.org/10.3390/rs13091727.

Zaussinger, F., Dorigo, W., Gruber, A., Tarpanelli, A., Filippucci, P., Brocca, L., 2019. Estimating irrigation water use over the contiguous United States by combining satellite and reanalysis soil moisture data. Hydrol. Earth Syst. Sci. 23, 897–923. https://doi.org/10.5194/hess-23-897-2019.

Zhang, K., Kimball, J.S., Running, S.W., 2016. A review of remote sensing based actual evapotranspiration estimation. WIREs Water 3, 834–853. https://doi.org/10.1002/wat2.1168.

Zhu, L., Suomalainen, J., Liu, J., Hyyppä, J., Kaartinen, H., Haggren, H., 2018. A review: remote sensing sensors. Multi-purposeful Appl. Geospatial Data. https://doi.org/10.5772/intechopen.71049.